ABSTRACT

Title of Document: SINGLE AND MULTI-DIMENSIONAL AAO TEMPLATE SYNTHESIZED HETEROGENEOUS NANOSTRUCTURES FOR ELECTROCHEMICAL ENERGY STORAGE

Stefanie Ann Sherrill, Doctor of Philosophy, 2012

Directed By: Dr. Sang Bok Lee, Department of Chemistry and Biochemistry

Anodic aluminum oxide (AAO) has been successfully used to fabricate a variety of well-ordered, regular nanostructured systems for a range of applications including electrochemical energy storage technologies. Template synthesized nanomaterials based on AAO can lead to well-designed nanoarchitectures composed of multiple favorable (high energy capacity, high electrical conductivity, strong mechanical strength) electrical energy storage materials and also one and three dimensional. Combining nanomaterials within a single system to form heterogeneous nanostructures leads to synergic effects unrealized with single components. Adding dimensionality to nanostructures potentially offers drastic improvements in both energy density and power density.

This dissertation describes the design, fabrication, and characterization of heterogeneous nanostructures based on AAO template synthesis methods for use as supercapacitor electrodes. The first approach utilizes two straightforward deposition techniques, atomic layer deposition and electrochemical deposition, for the construction of MnO_2/TiN nanotube arrays. Both the inner and outer surfaces of the nanotubes, where the charge storage takes place, are exploited for

enhanced capacitance. The second approach uses a novel well-ordered three-dimensional nanostructured template based on the modification of AAO during pore formation. A network of interconnecting pores is produced and demonstrates the controllable nature of AAO pore growth. An additional AAO modification to the pore barrier layer allows for electrical contact to the bottom aluminum substrate. The potential for new nanoarchitectures using the electrochemically modified AAO template, especially in multiple dimensions, is further realized using atomic layer deposition and chemical synthesis techniques.

SINGLE TO MULTI-DIMENSIONAL AAO TEMPLATE SYNTHESIZED HETEROGENEOUS NANOSTRUCTURES FOR ELECTROCHEMICAL ENERGY STORAGE

By

Stefanie Ann Sherrill

Dissertation submitted to the Faculty of the Graduate School of the
University of Maryland, College Park, in partial fulfillment
of the requirements for the degree of
Doctor of Philosophy
2012

Advisory Committee:
Professor Sang Bok Lee, Chair
Professor Neil Blough
Professor John T. Foukas
Professor Zhihong Nie
Professor Gary W. Rubloff

Dedication

I would like to dedicate this dissertation to my Mom, Dad and future husband Jimmy Wittenberg for their endless support.

Acknowledgements

I would like to acknowledge the tireless efforts of my adviser Dr. Lee and his guidance throughout my graduate career. His enthusiasm for science and innovative thinking inspire those around him. I would also like to thank Dr. Rubloff for being my unofficial co-adviser. His approach to the understanding of science has opened my eyes to creative thinking. Without any uncertainty, Liz Nguyen has been the most influential person to me these past five years. I would like to acknowledge her ability to motivate me to always search for answers. Her spirit makes those around her lively and she brought a sense of community to the Lee Lab. I would like to thank Dr. Izzy Perez for being my mentor and a great friend. Many thanks go to Dr. Parag Banerjee and Lauren Haspert for collaborating with me on projects. I would like to thank Jonathon Duay for being my 'go-to' guy for nearly all my questions. Thank you for your patience. I would like to thank Dr. Kim, Zhe Gui and Junkai Hu for their stimulating discussions and the current Lee group for their support. I would like to acknowledge the hard work of Dr. Ran Liu and Dr. Xia Bai. Your research provided an important foundation for the Lee group. I would like to thank the Rubloff group for their engineering perspective. Many thanks are owed to the Maryland Nanocenter staff for helping me become more knowledgeable about nanoscience fabrication and analysis.

I would like to thank the ARCS Foundation for their financial support for several years, which allowed me to focus on my research.

I would like to thank my family and friends for their continued support throughout this time. And last and certainly not the least I want to thank my future husband, Jimmy Wittenberg, for his patience and support.

Table of Contents

List of Tables

List of Figures

List of Illustrations

Chapter 1: Introduction to Electrochemical Energy Storage Technology

1.1 Background and Motivation

The current environmental impact from the world's dependence on fossil fuels is dire, resulting in an exhaustive list of damaging effects (acid rain, acidic oceans, urban air pollution, etc.). Future global success in energy will require a shift in energy usage away from fossil fuels.[1] Research is currently focused on developing renewable and sustainable technologies to capture and store energy to alleviate dependence on carbonized fuels. Renewable technologies such as wind power and solar power offer increased opportunities to explore diverse ways to capture energy. These energy sources, however, are unlikely to be the elixir for solving society's energy problems due to their high costs and inefficient delivery of energy. In the electric grid for example, energy is only captured during daylight hours for solar power or in the early morning hours for wind power when winds are at their peak. The largest demand for energy, however, occurs during the evening hours. Due to these variations in delivery rates, new technologies in electrical energy storage are needed in order to efficiently provide energy on demand to and store energy when in excess (i.e., uninterrupted power supply).[2] As a result, storage of electrical energy has become critical to solving our growing energy problems. Electrical energy storage systems, including lithium ion (Li-ion) batteries and supercapacitors offer vast potential for the ability to store and deliver energy efficiently and on demand, are therefore at the forefront of advancing technology. Continued advancements are needed in these energy storage systems to meet the current and growing demand for high energy density and high power density applications.[3] Advances in the smart grid, transportation sector (hybrid vehicles, commuter transportation, etc.)

and small electronics (tools and portable consumer devices), to name a few, will require efficient, low cost, and environmentally friendly electrical energy storage systems. To achieve these goals, current research is focused on novel materials, the integration of materials, and well designed architectures to enhance both energy and power density.

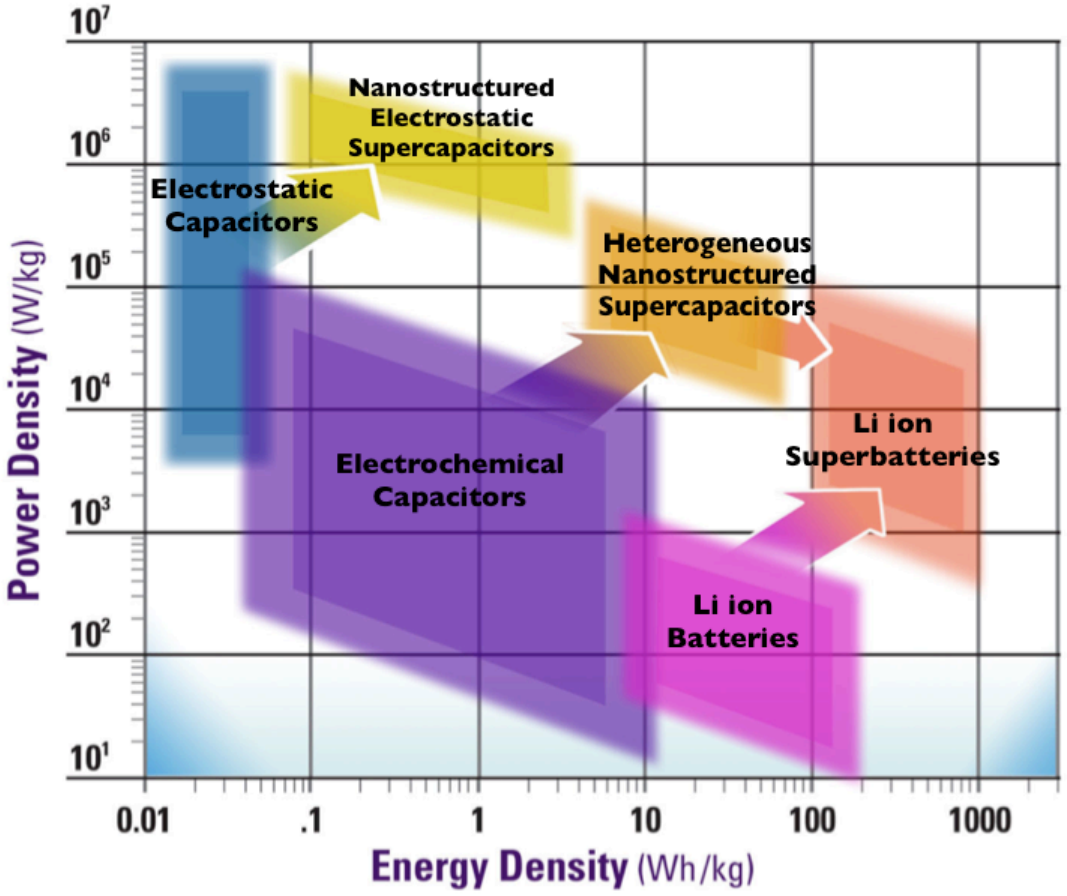

Figure 1.1 Ragone plot of power density (W kg^{-1}) versus energy density (Wh kg^{-1}) with current electrical energy storage technologies including conventional electrostatic capacitors, electrochemical capacitors, and Li-ion batteries. The extended shapes represent anticipated capabilities of electrical energy storage. (Adopted from EFRC: Science and Precision Multifunctional Nanostructures for Electrical Energy Storage 2008)

Electrical energy storage technologies are commonly compared on the Ragone plot as seen in Figure 1.1. The Ragone plot compares power density (W kg^{-1}) versus energy density (Wh kg^{-1}). Conventional capacitors with fast charging/discharging rates, have high power density yet fairly low energy density. Li-ion batteries, on the other hand, with the capacity to store a greater amount of energy, have high energy density yet low power density. Electrochemical capacitors or supercapacitors have moderate energy density and relatively high power density, bridging the gap between conventional capacitors and Li-ion batteries. Due to power requirements in a number of modern applications, which exceed the capabilities of the standard battery design, there has been a significant increase in the amount of attention for the high power capability supercapacitors. Advancing technologies aim towards both higher power density and higher energy density, shifting their capabilities towards the top right of the plot. It is often the case that a shift towards increased energy density comes at the expense of power density and vice versa.[4] Current research is aggressively aiming towards simultaneously achieving high power and energy density by incorporating novel materials, designing new architectures, integrating multifunctional materials and is particularly focused on these methods at the nanoscale.

Nanostructured electrical energy storage systems have gained a significant amount of attention in research as is apparent by the number of publications dedicated to nanomaterials and novel nanostructured architectures for the development of next-generation electrical energy storage. [5-7] Interest in nanomaterials and nanostructured designs stems from the unusual mechanical, electrical, and optical properties obtained by confining materials' dimensions. The advantages of these unique properties have been

explored for improving electrochemical capacitors, and therefore this chapter will focus its attention on electrochemical capacitors and the advance that come from confining the dimensions of electrode materials for electrochemical capacitors, integrating nanomaterials to design heterogeneous architectures, and finally the benefits of three dimensional nanostructures.

1.2. Electrochemical Capacitors

Electrochemical capacitors, often referred to as supercapacitors, were first reported in a 1957 patent obtained by Becker, who developed a high-surface-area carbon capacitor.[8] The first attempt to market supercapacitors was in the 1970s by SOHIO, who developed an aqueous-electrolyte-based supercapacitor for power saving units in electronics.[8] Supercapacitors received increased attention in the 1990s when they were considered for use in hybrid electric vehicles (HEVs). The U.S. Department of Energy developed a program to boost the power of existing batteries or fuel cells in the HEV by integrating supercapacitors to provide the power necessary for acceleration and also to take advantage of the regenerative braking system.[8]

Today supercapacitors are commercially available from companies such as Maxwell Technology, EPCOS, and Panasonic. Current applications for supercapacitors include the emergency door system in the Airbus A380[9] and powering commuter buses in Shanghai.[10] In these examples, companies have exploited the supercapacitors' ability to charge at fast rates and/or to last on standby for several hours. For example, the commuter buses utilize designated charging stations that also act as bus stops along the route. Within minutes the supercapacitors powering the buses are able to charge before the bus continues to the next stop. Certain disadvantages also exist, including any long

range commuting that may be necessary as well as considerations for when the bus is using maximum air conditioning.

There is a continued effort to increase the energy density of supercapacitors without sacrificing power density in order to achieve widespread use in day-to-day applications. Future use of supercapacitors may also lie in a hybrid design, integrating supercapacitors with advanced batteries to provide both high power and high energy density.[11] A fundamental understanding of supercapacitors and the methods in which they store charge is essential for the continued improvements of these systems. The basics of supercapacitor technology and recent developments to improve their overall performance are herein described.

Supercapacitors can be categorized into two main types based on their charge storage mechanism and the active materials commonly used to fabricate them.[7] The original supercapacitors patented by Becker are known as electrochemical double-layer capacitors (EDLCs), and are based on the energy stored at the double layer of the electrode/electrolyte interface.[8] The other type of supercapacitor is referred to as a pseudocapacitor (PC), which is based on fast, reversible Faradaic charge transfers at the surface of the active material. [3,8,12,13] The fundamental charge storage mechanism, materials used for both EDLCs and PCs, and recent developments of each type of supercapacitor are described below.

1.2.1 Electrical Double Layer Capacitor

The original type of supercapacitor, the EDLC, stores energy electrostatically in the double-layer as the charge separation forms at the interface of the solid electrode and the liquid electrolyte. [3,8,9] In 1853 Helmholtz discovered the existence of a double layer

and its characteristics at the electrode/electrolyte interface. The relationship of the double layer is described in equation 1.1

$$C = \frac{\varepsilon_o \varepsilon_r \cdot A}{d}, \qquad (1.1)$$

where capacitance (C) is a measure of the electrolyte dielectric constant (ε_r), the dielectric constant within a vacuum (ε_o), the surface area (A) of the electrode, and the distance (d) of charge separation. Later this model was refined by Gouy and Chapman as well as Stern and Geany, who suggested the existence of a diffuse layer in the electrolyte due to ion accumulation close to the electrode surface.[9] Figure 1.2 is a schematic of an electrical double layer within a full electrochemical cell. The positive and negative charges are attracted to opposite current collectors, creating charge separation. The applied voltage, load resistance and separator are also represented.

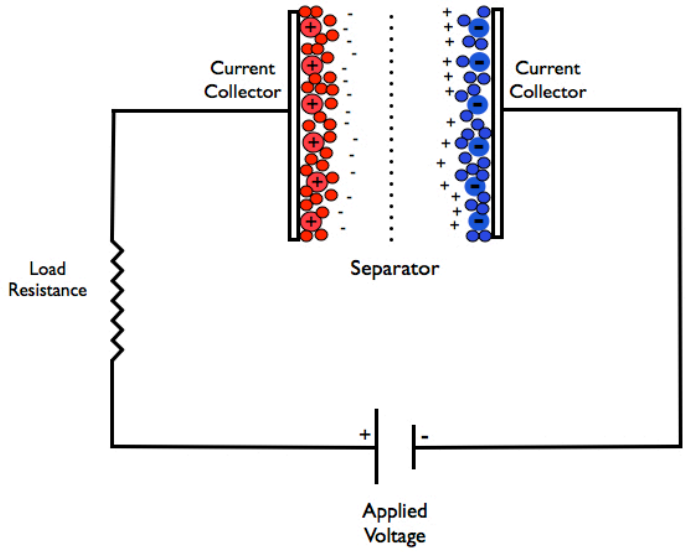

Figure 1.2 Electrochemical double layer capacitor cell setup.

According to equation 1.1, an increase in surface area will result in an increase in capacitance. This relationship is perhaps the key to the success of high-surface-area structures for EDLC technology. Since electrodes with extremely high surface area, such as porous carbon, are able to form a double-layer charge separation across the entire electrode surface area, extremely high capacitances are obtained.[8]

The second contributing factor to the success of EDLCs is their high reversibility.[2,9,14] EDLCs are able to charge and discharge at extremely high rates due to the charge storage mechanism which is solely based on physical relationship and is not associated with chemical or phase changes during cycling. EDLCs typically retain their capacitance over hundreds of thousands of cycles. The capacitance of EDLCs usually ranges from 15-50 $\mu m\ cm^{-2}$ in aqueous electrolytes.[14] The characteristics of the electrode material are the main contributing factor to capacitance in EDLCs. For example, pore size and total surface area have a direct effect on the capacitance.[3] One of the most common electrode materials in EDLCs is graphitic carbon, which satisfies all of the requirements for a well performing EDLC: high conductivity, electrochemical stability, and significant porosity.[9]

Carbon-based materials are currently some of the most widely used materials for EDLCs due to their favorable electrochemical properties, which help facilitate charge storage.[15-17] Activated carbons have demonstrated excellent charge storage capabilities due to the high porosity and increased surface area gained during the activation process.[18,19] Carbon aerogels have drawn increasing attention due to their extremely large surface area and controllable porosity.[20] The success of aerogels lies in their low ionic and electrical resistance.[7] Recently, Wang *et al.*[21] demonstrated superior high rate capabilities with a three-dimensional aperiodic hierarchical porous graphitic carbon (HPGC) material.

By combining macroporous cores, mesoporous walls, and micropores they have achieved energy and power densities as high as 22.9 Wh kg^{-1} and 23 kW kg^{-1}, respectively.

1.2.2 Pseudocapacitor

Supercapacitors also refer to devices such as pseudocapacitors (PCs), which unlike EDLCs, rely on fast, reversible Faradaic charge transfers at the electrode/electrolyte interface to store energy.[2,7] This Faradaic process allows PCs to achieve higher capacitances and energy densities than EDLCs. The Faradaic charge transfers are mainly redox reactions for which there exists a change in the oxidation state of the materials similar to a battery system. Capacitance can also occur from electrosorption and intercalation processes.[22] The charge storage mechanism for PCs has been well studied, however the complete mechanism is still not fully understood. It is well known that, similar to EDLCs, PCs also rely on high surface area electrodes and conductive materials to distribute and collect the electron current. The majority of the charge is transferred at the surface or within a few nanometers of the electrode/electrolyte interface rather than in the bulk of the electrode material.[2,3]

There has been significant research into electrode materials for pseudocapacitor devices in order to understand and enhance the overall capacitance of the energy storage system. To obtain pseudocapacitive behavior in supercapacitors, metal oxides are utilized as an electrode material. Currently, the greatest potential for achieving high energy density among metal oxides is realized with ruthenium oxide. [23-25] Hydrous ruthenium oxide has delivered some of the leading power and energy density results due to its high conductivity, multiple oxidation states, and superior cyclability. [25,26] Wu *et al.*[27] recently reported the fabrication of a hydrous RuO_2 nanotube arrayed electrode with

a high power density of 4320 kW kg^{-1} and moderate energy density of 7.5 Wh kg^{-1}. The mesoporous architecture, hydrous nature, and electronic conductivity of the electrode allowed for the rapid charging/discharging. However, because of the significant cost of ruthenium, several other promising metal oxides have been studied in detail such as manganese oxide, [28-30] vanadium oxide,[31] and nickel oxide. [23,32] By exploiting the structure and/or combining these metal oxides with other materials, metal oxides show great promise for the design of pseudocapacitors.

Conducting polymers offer another promising electrode material for obtaining high rate capabilities in pseudocapacitors. [33,34] Polymers such polyaniline, [35-37] polypyrrole,[38] and polythiophene[39] provide both relatively high conductivity and significant pseudocapacitive behavior due to their ability to oxidize and reduce at the electrode/electrolyte interface. Additional advantages of conducting polymers include facile polymerization techniques and low cost.[40] Lee *et al.*[41] reported the fast charging/discharging of poly (3,4-ethylenedioxythiophene) (PEDOT) nanotubes that achieved high power density of 25 kW kg^{-1} while still maintaining 80% of their energy density (5.6 Wh kg^{-1}).

1.3 Nanostructuring Supercapacitors

Many of the supercapacitor examples discussed thus far have underlined a growing trend in advancing electrical energy storage: nanostructuring electrode materials for achieving high power densities and high energy densities. As mentioned previously, the unique benefits of nanostructured materials include enhanced electrical, mechanical, and optical properties. Nanostructured electrode materials have an increased electrode/electrolyte interface compared to their bulk counterparts, which leads to higher

rate capability for supercapacitors, especially compared to their bulk counterparts. The short diffusion path for electronic transport allows for operation with low-electrical-conductivity materials or at a high power rate. The narrowly spaced interfaces can also result in high power density due to the reduction of the effective diffusion path length.[7,42,43] Despite these many advantages, however, it's important to consider the drawbacks of nanosizing electrode materials, such as low packing densities, which leads to lower volumetric energy density and also increased technical challenges for the syntheses of these electrode materials.[7]

Fischer *et al.*[44] recently demonstrated both high areal and volumetric capacitance for nanoscale MnO_2 within ultraporous carbon nanofoams. The conformal, nanoscopic deposits of birnessite ribbons and amorphous MnO_2 throughout the carbon structure provided intimate contact between the carbon and oxide material. In another example, Biswas *et al.*[45] fabricated multilayered, nano-architectured graphene nanosheets. The nanosheets exhibited excellent capacitance due to their flexible design whereby the particle size, surface area, and edge chemistry were easily controlled.

1.4 Heterogeneous Nanostructures for Electrical Energy Storage Technology

One of the most impressive recent improvements of electrical energy storage technology arises from the combination of favorable electrode materials to deliver high-rate capabilities and increased energy capacity.[42] The development of heterogeneous supercapacitors is centered on the ability to combine two or more electrode materials into a single system to produce increased power and energy.[46] The limitations of each individual electrode material is met by the integration of one or more electrode materials, each intended to address a different demand.[47] For example, researchers have

successfully increased the overall performance of an energy system by combining metal oxide materials such as ruthenium oxide and manganese oxide with carbon-based materials. [48-50] The limitations of frequently used metal oxides, such as low conductivity and weak structural design, were met by the superior conductivity and mechanical strength of metals and carbon-based materials such as carbon nanotubes. [51,52] Liu *et al.*[53] reported similar success when combining ruthenium oxide and PEDOT into arrays of nanotubes. The combination of these materials yielded power and energy densities of 20 kW kg^{-1} and 28 Wh kg^{-1}, respectively. The RuO_2/PEDOT nanotube arrays were characterized using a symmetrical setup whereby both electrodes were made up of RuO_2/PEDOT. Similar success was demonstrated by combining PEDOT with MnO_2 in both a coaxial nanostructure[54] and a composite nanostructure design whereby the PEDOT nanowires were enriched with MnO_2 nanoparticles.[55] Despite these recent achievements, the full potential of supercapacitors has yet to be realized and may possibly lie in the combination of multi-functional, multi-dimensional nanostructures that yield the largest increase in both power and energy density.

1.5 Multi-dimensional Nanoarchitectures for Optimal Energy Storage

The architectural design of heterogeneous nanostructures must be carefully considered when determining the ideal structure for achieving optimal power and energy density. Recent work[42] has described in detail the advantages that electrode materials possess when they are designed from zero-dimensional structures such as nanoparticles to three-dimensional (3D) arrays of nanostructured networks. An electrode material's properties can be dramatically enhanced if the appropriate nanostructure is chosen. For example, one-dimensional (1D) nanostructures, structures that contain of at least one

dimension between 1 and 100 nm, benefit from the direct pathway for efficient charge transport along its micro-scale axis. 1D metal-carbon hybrid nanostructures were formed using *in-situ* fabrication of Co_3O_4 or Pt nanocrystals distributed homogeneously within carbon frameworks.[56] In this work, Liang *et al.* utilized an alumina template to control the distribution of nanocrystals within the nanoporous carbon. The 1D hybrid nanostructure shows superior specific capacitance of 1066 F g^{-1}. 1D nanostructures have several disadvantages, as discussed below, and therefore continued growth in other dimensions may overcome these shortcomings.

3D structures may well hold the future to next-generation supercapacitors.[4] In order to progress into a new performance growth curve, a shift in dimensionality is required. The key advantages to these 3D nanostructures lie in the short transport lengths for ions in the solid-state electrode in addition to the small areal footprint. What is of particular interest, unfamiliar in other nanostructures, is the fully interconnected pore structure that facilitates solvent infiltration, ion transport and product mass transport. The use of appropriate building blocks is essential in which the void space as well as the electrode structure is considered. To achieve high quality modifications of 3D architectures, the nature of the void or 'nothing' space is one of the key considerations especially when pore size is below 100 nm. Many challenges remain for the design of 3D nanostructured electrode systems including the characterization and understanding of the electrochemical interactions, physical and chemical properties and the disordered nature of the solid phase. [4,57]

1.6 Template-Synthesized Nanomaterials

The fabrication of simple to complex multi-dimensional structures can be accomplished using template-synthesized nanomaterials. Designing supercapacitor electrode materials or even full electrochemical cells based on a well-structured template can provide vast improvements in electrochemical energy storage. Template synthesized nanomaterials typically exhibit properties such as high surface area electrodes, large surface to volume ratios, and favorable structural stability. These characteristics may very well lead to both fast ion and electron transfers, intimate contact between electroactive materials and the electrolyte, and improved flexibility. Advantage of designing electrode materials based on templated nanomaterials is the variety of materials that can be employed as templates, such as inorganic/organic compounds, polymers, and even biological materials. Template-synthesized nanomaterials can also provide an array of electrode materials with diverse compositions, structures, and morphologies. [58,59]

One of the pioneers in the effective use of template-synthesized nanomaterials was Martin[60] who demonstrated the generation of nanomaterials for a diverse array of applications. For example, Martin and co-workers fabricated freestanding nanoporous carbon membranes and carbon nanotubes using a chemical vapor deposition (CVD) technique combined with anodic aluminum oxide (AAO). These template prepared nanotubes exhibited a high Li-ion intercalation capacity of 490 mAh g^{-1} and showed that a tube-within-tube design leads to capacities at least two times higher.[61]

The AAO template mentioned previously has been also used to develop heterogeneous nanostructures for electrochemical energy storage. Liu *et al.*[62] have exploited the high surface to volume ratio, facile fabrication, and cost-effective technique

of AAO to fabricate a variety of AAO-templated nanostructures including coaxial MnO_2/PEDOT nanowires,[62] concentric RuO_2/PEDOT nanotubes,[53] and PEDOT nanowires enriched with MnO_2 nanoparticles[55] for improving supercapacitor performance. Recently, the AAO template has been used to combine multiple deposition techniques including atomic layer deposition and electrochemical deposition within the nanostructure to fabricate supercapacitor electrodes, as discussed later in Chapter 3.[63]

Template-synthesized materials not only provide the framework for 1D nanostructures, but also enable the design of two-dimensional films, and 3D nanostructured networks. These structures, with careful control of pore arrangement and size, are nearly unobtainable without the use of a template. For example, Shi *et al.*[64] reported the growth of TiO_2 nanorods in 3D confined spaces using a pulsed CVD method and AAO template for confined, well controlled nanochannels. More recently, Wei *et al.*[65] prepared 3D pillared porous carbon nanosheets using supporting carbon pillars between the carbon layers. They utilized MgO templates and the carbonization of pitch to show that the unique structure allowed for a high transport rate of electrolyte ions and electrons through the electrode matrix. Cao *et al.*[66,67] used CVD to prepare 3D graphene networks to construct graphene/NiO supercapacitor electrodes that demonstrated high specific capacitance of 816 F g^{-1} at 5 mV s^{-1} and respectable cycling performance. In Chapter 4 I discuss, 3D networks of nanomaterials fabricated based on the exploitation of the AAO template and illustrate a novel technique to obtain interconnecting electrode materials for supercapacitors. In the Chapter 2, the focus will remain on the AAO template for the design and fabrication of nanomaterials and the characterization techniques used to understand the diverse properties of nanomaterials.

1.7 Overview of Dissertation

This dissertation describes the design, fabrication, and characterization of template-synthesized nanomaterials for use as supercapacitor electrodes. The three major objectives include:

(1) the combination of self-limiting atomic layer deposition with electrochemical deposition within an AAO template

(2) the enhanced capacitance of supercapacitor electrodes based on AAO-based heterogeneous nanostructures, and

(3) the modification of AAO for the development of novel, well-ordered 3D interconnecting nanostructures.

In Chapter 2, the AAO template is described in detail to illustrate the pore formation mechanism, general structure, and characteristics of AAO. This Chapter also includes analytical techniques for the structural and electrical analysis of nanomaterials. Chapter 3 reveals the construction and characterization of MnO_2/TiN nanotube arrays that satisfy the first and second objective. In Chapter 4, I describe a well-ordered 3D nanoporous network consisting of interconnecting pores from the modification of AAO during pore formation. Chapter 4 also describes an additional AAO modification that allows for direct access from the nanopore to the bottom aluminum substrate, thus providing electrical contact for further fabrication. In the final Chapter of this dissertation the conclusions and outlook are discussed.

Chapter 2: Fabrication and Characterization of AAO Template Prepared Nanomaterials

2.1 Introduction

One are on which recent scientific advances have focused is the ability to create precise systems. The widespread fabrication of microelectromechanical systems (MEMS) and other microscaled structures has taken full advantage of 'top-down' techniques such as lithography that provide micro and nanoscaled materials for a variety of applications. These patterning techniques create well-defined templates for fabrication of various nanostructures. Conventional lithography, however, is limited for materials with dimensions below 100 nm. Also, due to high fabrication costs of lithography-based structures many researchers are looking for other templated structures with controllable dimensions and cost-effective procedures. For the development of precise nanostructures with dimensions of less than 100 nm, techniques must be employed with more sophisticated facilities.[58] Template synthesis provides a shift in focus to more self-organized nanostructures with periodic arrangement of nanopores. Anodic aluminum oxide (AAO) is at the forefront of advancements in template prepared nanomaterials. Herein, the fabrication and characterization of nanomaterials based on the AAO template is described.

2.2 Background and Motivation: AAO

Research has focused on providing a combination of nanotechnology and surface engineering to fabricate various nanomaterials and novel nanostructures. Frequently, cost-effective techniques and straightforward designs for commercial viability become the focus of advancing technology. AAO, an alumina membrane prepared from basic

electrochemical methods, provides a unique, inexpensive, and highly controllable nanoporous template structure for the design and fabrication of nanomaterials through 'template synthesis.'[58] AAO consists of a densely packed hexagonal array of nanopores assembled during the anodization of aluminum. The precise control of AAO surface geometries has resulted in the fabrication of novel and unique nanostructures. AAO is perhaps one of the most widely studied methods for the synthesis of ordered nanostructures for its potential in a variety of applications.

2.3 The Design and Fabrication of AAO

The anodization of Al to form porous AAO is an electrochemical process whereby the formation of a densely packed hexagonal array of nanopores is completed. The formation of nanopores is a self-organized, self-assembling multistage process consisting of a pre-treatment, anodization, and post-treatment steps. The pre-treatment of Al includes the degreasing and electropolishing of Al to obtain a nearly defect free Al surface. The anodization step, whereby the growth of oxide occurs, is the main process to form the Al oxide porous structure. Anodization of Al can occur in a variety of electrolyte solutions and at coordinating applied potentials for the self-ordering fabrication regime of AAO. The most commonly used acidic electrolytes include oxalic acid, phosphoric acid and sulfuric acid, which can provide a range of dimensions for the growth of nanoporous structures. Post-treatment steps include adjusting the pore diameter and removal of the Al and/or the alumina base, all performed with a basic chemical wet etching process.

Self-Assembly of Nanopores:

AAO is formed using either an constant applied current or constant anodizing potential. More recently, the constant potential method has been used to fabricate highly ordered AAO films. This method is actively used in our research lab, and so therefore will be my focus here. To understand the self-assembly phenomena of AAO one can take a closer look at the anodization parameters. The observed relationship between current density and time under constant potential is a result of two separate processes, as shown in Figure 2.1. The first process is an exponential decrease in current, due to barrier layer formation (dotted line) and the second process is the pore formation (dashed line).

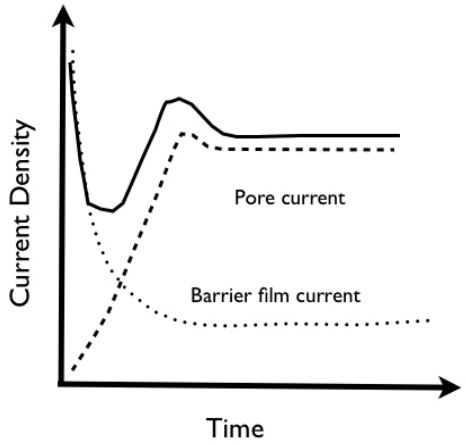

Figure 2.1 Schematic diagram of the effects that overlapping processes that occur during porous oxide growth under constant anodization voltage have on the current density (Adopted from Hoar *et al.*[68]).

During pore formation under steady-state growth conditions all reactions occur at the pore bottom and the barrier layer. The barrier layer is the bottom oxide layer, which has nearly identical oxide characteristics to the pore walls. Here, the maximum electric field is present and ions drift across the barrier layer reacting at the aluminum/oxide interface

and the oxide/electrolyte interface as shown in Figure 2.2. In this barrier layer region, two sets of ion migration occur. Al^{3+} ions drift in the direction of the oxide/electrolyte interface followed by transfer into the electrolyte. This process results in the dissolution of alumina film as seen in equation 2.1

$$Al_2O_3 + 6H^+ \rightarrow 2Al^{3+}(aq) + 3\,H_2O \quad (2.1)$$

The other ion migration process is movement of the O^{2-}/OH^- ions towards the aluminum/oxide interface. It is generally accepted that one of the ion species (O^{2-}/OH^-) reacts with the available Al atom to form alumina as shown in equation 2.2

$$2Al + 6OH^- \rightarrow Al_2O_3 + 3H_2O + 6e^- \quad (2.2)$$

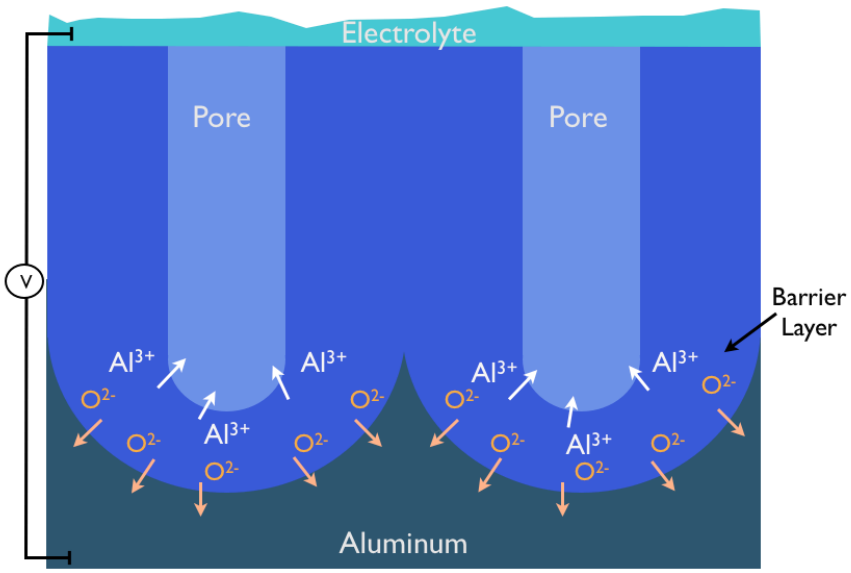

Figure 2.2 Schematic showing the ion migration of Al^{3+} and O^{2-} within the AAO barrier layer during pore formation.

During steady-state pore growth, the above reactions occur simultaneously. The dynamic equilibrium caused by the equal rates of oxide growth (aluminum/oxide interface) and oxide dissolution (oxide/electrolyte interface) permits the self-assembly of AAO.

The mechanism of self-assembly in AAO has been well studied and several theories are explained elsewhere to the nature of this process.[58] Two of the prevalent theories are described here briefly. Chen *et al.*[69] proposed a basic electrostatic model of the field-assisted dissolution and growth rates of the barrier layer. They represented the electric field at the two interfaces using simple electrostatics, as shown in equations 2.3 and 2.4

Aluminum/oxide interface: $$E_{AO} = \frac{r_{pore}}{r_{pore} + D_{BL}} \cdot \frac{V}{D_{BL}} \quad , (2.3)$$

Oxide/electrolyte interface: $$E_{OE} = \frac{r_{pore} + D_{BL}}{r_{pore}} \cdot \frac{V}{D_{BL}} \quad , (2.4)$$

where E_{AO} and E_{OE} represent the electric field for the aluminum/oxide interface and oxide/electrolyte interface, respectively. The pore radius (r_{pore}), barrier layer thickness (D_{BL}), and potential (V) are shown. These equations suggests that when the pore radius (r_{pore}) decreases from its equilibrium value, the electric field at the oxide/electrolyte interface increases, causing the field-assisted dissolution rates to increase. The dissolution rate increase thus causes an increase in the pore radius. A similar result could occur with changes in D_{BL}. This model therefore describes a self-adjusting behavior and suggests morphological changes to the pore bottom lead to electric field changes that counteract the physical change.

The second theory uses the mechanical stress and volume expansion associated with AAO pore formation as the basis of self-assembly and ordering, as provided by Jessensky[70] and Nielsch.[71] Their model suggests that anodization of alumina creates

volume expansion due to the intimate contact of alumina and Al. The model also argues that because pore formation occurs on a planar substrate with all pores growing simultaneously, that the formation can only preceed vertically. This expansion causes mechanical stress in between the pore walls. The balance of the stress leads to the self-ordering behavior of AAO. Nielsch *et al.*[71] additionally showed that the best ordering of pores occurs when moderate increases in volume change occur (~1.2x original volume).

General Structure of AAO

AAO's unique formation allows for highly controllable dimensions to form closed-packed arrays of pores. The pores are embedded in a hexagonal cell structure composed of alumina. The nanopores run parallel along the thickness of the template. The bottom of each pore, where anodization is terminated, is a hemispherically shaped structure known as the barrier layer, as previously described. In general, the structure of AAO is characterized by parameters such as pore diameter, interpore spacing, barrier layer thickness, and wall thickness.[58] Each of these parameters depends on the anodization process as described below and as depicted in Figure 2.3

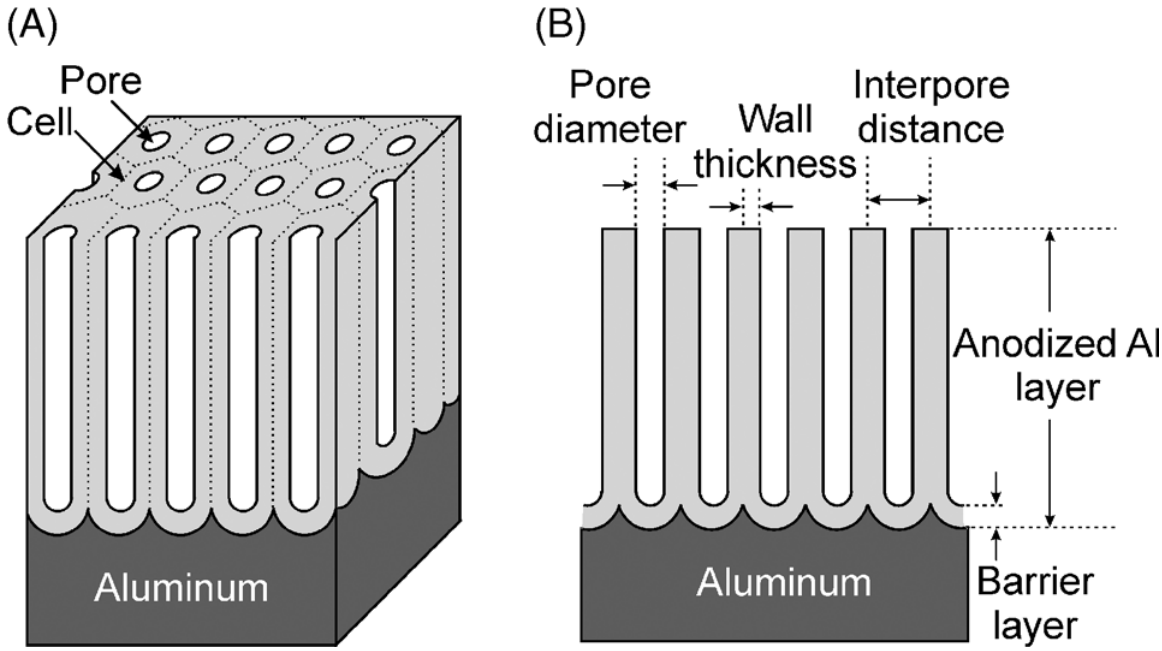

Figure 2.3 (a,b) Schematic showing the alumina nanopores and their associated parameters (pore diameter, wall thickness, interpore distance, barrier layer, etc.) (Reprinted with permission, Wiley-VCH, Eftekhari, 2008).

Pore Diameter

The pore diameter (D_p) is proportional to the anodizing potential with a related proportionality constant λ_p as shown in equation 2.5:[72]

$$D_p = \lambda_p \cdot U \quad , \quad (2.5)$$

where U is the applied potential. During early studies of AAO based research, it was believed that the pore diameter was independent of the applied forming potential. In later studies, however, it was determined that the pore diameter was dependent on the anodizating potential or current density based on:[72]

$$D_p = D_c - 2 \cdot W = D_c - 1.42 \cdot B = D_c - 2 \cdot W_U \cdot U \quad , \quad (2.6)$$

where D_c is the interpore distance (nm), W is the wall thickness (nm), B is the barrier layer thickness (nm), and W_u is the wall thickness per volt (nm V^{-1}). It is also interesting to note that the pore diameter does not change significantly with anodization time. [73,74]

Interpore Distance

The interpore distance (D_c) is generally accepted to be proportional to the forming potential of steady-state growth with a proportionality constant λ_c of approximately 2.5 nm V^{-1}:[71]

$$D_c = \lambda_c \cdot U \quad , \quad (2.7)$$

Figure 2.3 illustrates the location of the interpore distance as the distance between the outer walls of a single pore.

Barrier Layer Thickness

During anodization a thin compact barrier layer is formed at the pore bottom/electrolyte interface and is continuously dissolved by locally increased field. A new barrier layer at the metal/oxide interface is then reconstructed. This barrier layer oxide has the same character as an oxide formed in the atmosphere and allows the passage of current only due to exiting faults in its structure. The barrier layer thickness is directly dependent on the anodizing potential (~ 1.15 nm V^{-1} for porous AAO).[75]

Wall Thickness

The wall thickness is generally described based on a thickness (nm) per volt measurement, although some research has shown that it varies with certain electrolytes and potential ranges. The wall thickness is represented in Figure 2.3 and can be calculated based on the transformation of equation 2.5 with equation 2.8

$$W = \frac{D_c - D_p}{2} \quad , \quad (2.8)$$

AAO was initially created with a simple, one-step anodization procedure. In 1995, Masuda *et al.*[76] reported a two-step anodization process, which resulted in a more highly ordered arrangement of nanopores. After the initial anodization step that forms a somewhat ordered nanostructure surface, the alumina is chemically etched away in acidic solution leaving an Al surface with an arrangement of peaks. The second anodization is carried out with the same anodization parameters as the first anodization step, resulting in highly ordered parallel nanopores due to the initial 'peaked' surface created during the first anodization.

Modifying the AAO Porous Structure

For the continued use of AAO for novel nanostructures, research has focused on influencing the porous structure of AAO to produce unique architectures. For example, Tian *et al.*[77] reduced the voltage during anodization by a factor of $1/\sqrt{2}$ after the second anodization. The result was Y-branched, ramified pores occurring at the same depth as the original pore structure. Modified template structures such as these were fabricated for their potential use in two-dimensional photonic devices. Recently, Ajayan *et al.*[78] reported the synthesis of multiply connected and hierarchically branched nanopores inside AAO. Due to the high controllability of the nanoporous structure, they fabricated a large variety of complex, branched nanostructures and demonstrated a powerful approach to producing a template with greater morphological complexity. Yi *et al.*[79] demonstrated the non-uniform thinning of the barrier layers that resulted in tree-like

morphology of branched channels, again demonstrating the high controllability of branched channels, especially on a large scale.

2.4 Nanomaterials Based on AAO

The use of AAO as a template for the synthesis of nanomaterials provides a powerful and cost-effective method. In general, AAO can be used to engineer nanomaterials in two main routes; (1) the Al oxide film with the remaining Al substrate can be used directly for the deposition of materials, and (2) the Al oxide can be separated from the Al and be further processed into a freestanding membrane with open pores at the top and bottom of the nanostructured membrane.[58] A considerable amount of research has been dedicated to the fabrication of nanomaterials based on AAO for the formation of nanostructures including metal oxide nanodots,[80] carbon nanotubes,[81] and inorganic/organic nanowires[82,83] and nanotubes[84] to name a few. This Chapter will focus on two main deposition techniques and current analytical tools to investigate the properties of nanomaterials.

2.4.1 Electrochemical Synthesis of Nanomaterials

Electrochemical synthesis or electrochemical deposition (ECD) is defined by the diffusion of charged species through an electrolyte when an external electric field is applied. The process of converting electrical energy into chemical energy in this setup is referred to as electrolysis. Electrolysis occurs within an electrolytic cell the typically has two electrodes connected to the power supply. The electrode where oxidation proceeds is connected to the positive side and is referred to as the ‘anode.’ The electrode where reduction takes place is the negative side or the ‘cathode.’ When ECD takes place on the anode by an oxidation reaction it is called anodic deposition.[59]

ECD is commonly used in industry for coating metals and is sometimes referred to as electroplating. The deposition takes place on conductive substrates such as metals, alloys, or semiconductors. Electrochemical deposition is used in many applications including microelectronics,[85] biosystems,[86] and energy storage devices. [87,88] There are many advantages to depositing materials with ECD, including obtaining intimate contact with the conductive material and the low cost of the materials. The deposition process is straightforward and the materials are usually readily available. ECD is also advantageous for depositing materials into 3D geometries, especially at the nanoscale.[89] By depositing material with ECD, one has the ability to control the kinetics and thermodynamics of the system by controlling either the current passed or the applied cell potential, respectively. The composition and morphology of the material can be controlled by changing the electrolyte composition and other electrochemical parameters. Cho *et al.*[41] showed the precise control of poly (3,4-ethylenedioxythiophene) (PEDOT) deposition by controlling the applied potential and monomer concentration during ECD. They observed a change from PEDOT nanowires to a nanotubular shape by altering the voltage by only a few tenths of volts.

ECD commonly uses two main methods for depositing materials. The potentiostatic method (chronoamperometry /chronocoulometry), which applies a constant potential during deposition, controls the process thermodynamically. One can observe the current and charge throughout the synthesis process. The second deposition method, referred to as galvanostatic deposition, uses kinetic control through a constant current technique. The potential change can be monitored during this method of deposition.[59]

Metal oxides are commonly electrochemically deposited within the AAO template or on planar substrates. One representative deposition technique is based on anodic oxidation in which the metal ion in the electrolyte solution is in a lower oxidation state and is oxidized to a higher oxidation state. During this deposition process, the pH of the electrolyte maintains stability of the lower oxidation state ion while the higher oxidation state ion undergoes hydrolysis to produce a metal oxide or hydroxide. The example below, equations 2.9 and 2.10, shows the anodic deposition of a generic metal oxide.

$$M^{z+} \rightarrow M^{(z+\Delta)+} + \Delta e\text{-}, \quad (2.9)$$

$$M^{(z+\Delta)+} + (z+\Delta)OH^- \rightarrow M(OH)_{z+\Delta} \rightarrow MO_{(z+\Delta)/2} + (z+\Delta)/2H_2O, \quad (2.10)$$

2.4.1.1 General Setup for Three Electrodes in Electrochemical Cells

Electrochemical deposition is typically performed in a three-electrode cell setup that includes a working electrode, a counter electrode, and a reference electrode. The working electrode consists of a conductive substrate where the deposited material is formed. Figure 2.4a shows a typical three-electrode cell setup with a working electrode, a counter electrode (Pt), and a reference electrode (Ag/AgCl). Figure 2.4b below depicts a working electrode setup in which the exposed window defines the area where the material is to be deposited. The conductive substrate (TiN nanotubes) is connected externally, usually with conductive adhesive.

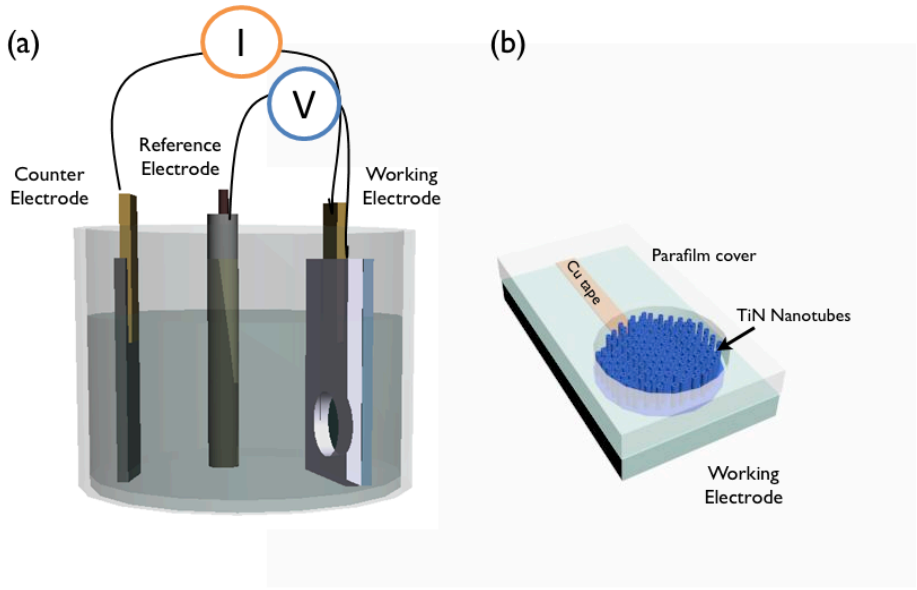

Figure 2.4 3D images showing (a) a typical three-electrode cell setup including reference electrode, counter electrode and working electrode and (b) sample holder that exposes the working electrode to the electrolyte in a well-defined area.

2.4.2 Atomic Layer Deposition

Atomic layer deposition (ALD) is increasingly being used as a technique for deposition of nanomaterials into high-aspect-ratio nanostructures such as AAO.[90-92] This gas phase deposition technique is ideal for depositing thin, conformal films within nanostructures due to its ability to control its dimensions with atomic level precision even at high aspect ratios. ALD can currently deposit a wide variety of materials, including metals,[93] oxides,[94,95] and nitrides.[96] It is commonly used to form nanotubes[97] and nanowires [98] within AAO structures. These nanostructures have been analyzed using TEM[99] and other imaging analysis and show excellent conformality. Atomic layer deposited nanomaterials and other ALD processed structures are being used for

applications in semiconductor,[100] MEMS,[101] bio-engineering,[102] and energy storage devices[63,90].

2.4.2.1 General Setup for Atomic Layer Deposition

ALD uses self-limiting chemistry in a layer-by-layer fashion to control the thickness of films. A typical ALD cycle involves two half reactions with two gaseous precursors that react with the exposed surface chemistry individually. Once all reaction sites of the substrate are saturated, the remaining molecules are purged out of the chamber. Figure 2.5 shows a typical oxide film formation including the four main steps of an ALD cycle. After the first precursor is exposed and reacts with the substrate surface, the excess molecules are purged out of the chamber with an inert carrier gas (N_2, Ar,..). The second reactant or precursor is then introduced into the chamber and reacts with the new surface chemistry. After a second purging process, a single ALD cycle is then complete and a single monolayer has grown. This cycle can be repeated to a desired thickness forming multiple layers on the substrate. A sample baseline recipe for the Beneq TFS-500, a commercially available ALD reactor, is provided in the appendix (A.1).

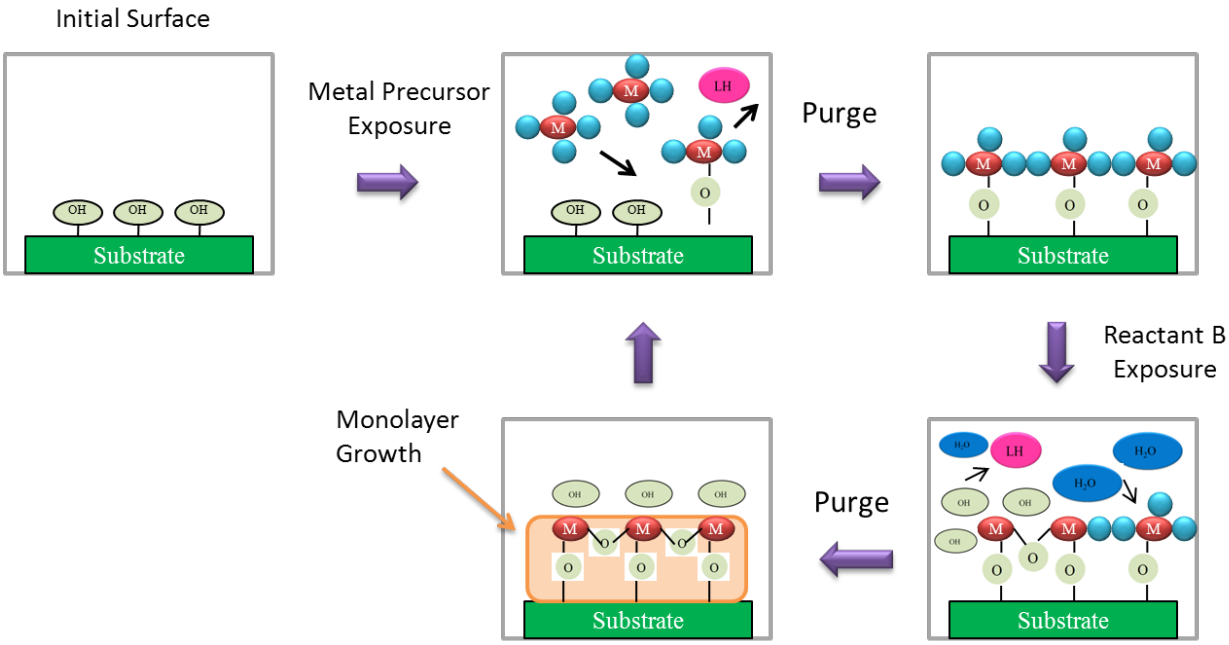

Scheme 2.1 Schematic of an ALD cycle illustrating the introduction of two gaseous precursors and purging steps in between to form a monolayer on the substrate surface

2.5 Characterization of Nanomaterials

The progress of nanotechnology has required the invention of new analytical techniques to analyze materials on such a small scale (1-100 nm). The study of nanomaterials presents new opportunities to enhance how materials are measured and analyzed. Here I discuss structural and electrical techniques for the characterization of nanomaterials.

2.5.1 Structural Characterization

Nanomaterials can be characterized based on their structural and chemical properties. Relatively new technologies along with well-developed chemical analysis techniques are employed to determine characteristics such as morphology, size, chemical nature, and crystallinity.

2.5.1.1 Electron Microscopy

With the development of electron microscopy, nanomaterials could be visualized for the first time, providing analysis of their physical structures and properties. Scanning electron microscopy (SEM) and transmission electron microscopy (TEM) are the two main microscope techniques used to perform structural investigations of nanomaterials.

SEM provides an image of a sample's surface by scanning it with a high-energy beam of electrons in a raster scan pattern. The atoms that make up the sample interact with the electrons producing signals that provide information about the sample's surface topography, composition, and other properties. SEM can produce very high-resolution images of a sample's surface often reaching 1 nm resolution. Magnification can operate over a range of up to six orders of magnitude, from 10 to 500,000 times. Sample preparation is a relatively straightforward process in which a sample of appropriate size is mounted rigidly onto a specimen holder. Samples are typically electrically conductive or electrically grounded to prevent the build up of electrostatic charge at the surface.

TEM provides a slightly different physical analysis of nanomaterials including modulations in chemical identity, crystal orientation, electronic structures and sample-induced electron phase shift. TEM operates using a beam of electrons that is transmitted through a thin specimen, interacting with the specimen as the electrons pass through. From this interaction, an image is formed, which is magnified and focused onto an imaging device such as a fluorescence screen, a photographic film, or is detected by a sensor such as a CCD camera. TEM requires a potentially time-consuming sample preparation process whereby the sample is prepared on a standard size grid. Sample

preparation is specific to the material under analysis and the desired information to obtain from the sample.

While using electron microscopy, one can typically take advantage of a chemical analysis technique known as energy dispersive x-ray spectroscopy (EDS). EDS is an analytical technique used for the elemental analysis or chemical characterization of nanomaterials. It utilizes x-rays emitted from the specimen when bombarded with electrons to identify the elemental composition of a sample. As the electron beam transmits the electrons to the sample, electrons are ejected from the atoms of the samples surface. This process leaves an electron vacancy, which is filled by an electron from a higher shell, emitting an x-ray to balance the energy difference between the two electrons. An x-ray detector measures the energy of emitted x-rays, which is virtually unique to each element. The resulting information is provided in a spectrum of the energy versus relative counts of the detected x-rays, providing both qualitative and quantitative data. The accuracy of EDS can be affected by factors including the overlapping peaks of some elements, the energy of the x-ray and the density of the material.

2.5.2 Electrical Characterization

Electrical characterization of nanomaterials, particularly for those used as electrical energy storage systems allows for side-by-side comparisons of a variety of nanomaterials. Cyclic voltammetry (CV) and galvanostatic (GV) charging/discharging cycling techniques are perhaps the most common electrical testing performed with supercapacitor systems. In this dissertation, a three-electrode cell system is used to complete both CV and GV cycling testing. Three-electrode cells differ from typical two-

electrode cells and packaged cell testing in several aspects. In a three-electrode cell configuration, only one electrode (referred to as the working electrode) contains the material under investigation. When a voltage is applied to the working electrode it is with respect to the reference electrode. As a result, the potential range for the working electrode of a three-electrode cell has twice the potential range as is applied to the two-electrode cell, leading to double the capacitance. This factor is potentially important when comparing the power and energy density of supercapacitors given their relationship to the voltage window. For example, energy density (E_d) is calculated based on the capacitance (C) and voltage (V):

$$E = \frac{1}{2}CV^2 \quad , \ (2.11)$$

If the capacitance and voltage window are not carefully considered, the calculated energydensity maybe overestimated. Although CV and GV cycling testing for packaged supercapacitors is well developed, it is often impractical for scientists to assemble full sized, packaged cells to test electrode materials. It is fairly common practice for research to focus on the intrinsic properties of the electrode materials of supercapacitors and therefore the information from CV and GV cycling based on three-electrode cells remains valuable.[103]

2.5.2.1 Cyclic Voltammetry

Cyclic voltammetry is a type of potentiodynamic electrochemical measurement commonly used to analyze the electrical properties of supercapacitors. During a CV cycle, the working electrode potential is ramped linearly versus time, similar to linear sweep voltammetry. When the CV cycle reaches a set potential the working electrode's potential ramp is inverted and can be repeated multiple times for a given experiment.

The CV plot shows the current versus the applied voltage. For supercapacitors, the capacitance can be calculated based on this current and the scan rate:

$$C = \frac{i}{\frac{dv}{dt}} \quad , \quad (2.12)$$

An ideal supercapacitor will exhibit a square shaped CV curve, but due to internal resistance, the CV curve usually deviates from this shape.

2.5.2.2 Galvanostatic Charging/Discharging Cycling

Galvanostatic (GV) charging/discharging cycling curves are obtain from applying a constant positive current to charge an electrode (charging), and then applying a constant negative current to discharge an electrode (discharging). A GV cycling plot displays the applied potential versus time. Capacitance can be determined based on the slope of the curve:

$$C = \frac{i \cdot t}{V} \quad , \quad (2.13)$$

Ideal supercapacitors exhibit symmetrical curves for both charging and discharging. Deviation from symmetry is due to internal resistance of the electrode.

2.5.2.3 Four-Point Probe Measurements

Four terminal sensing or four-point probe measurements are electrical impedance measurements that use separate pairs of current-carrying and voltage sensing electrodes (Figure 2.5). The four-point probe is commonly used to determine sheet resistance of conductive thin film materials with nominally uniform thickness. To perform a sheet resistance measurement, a DC current is applied between the outer two current probes and the voltage is measured in the inner two probes.

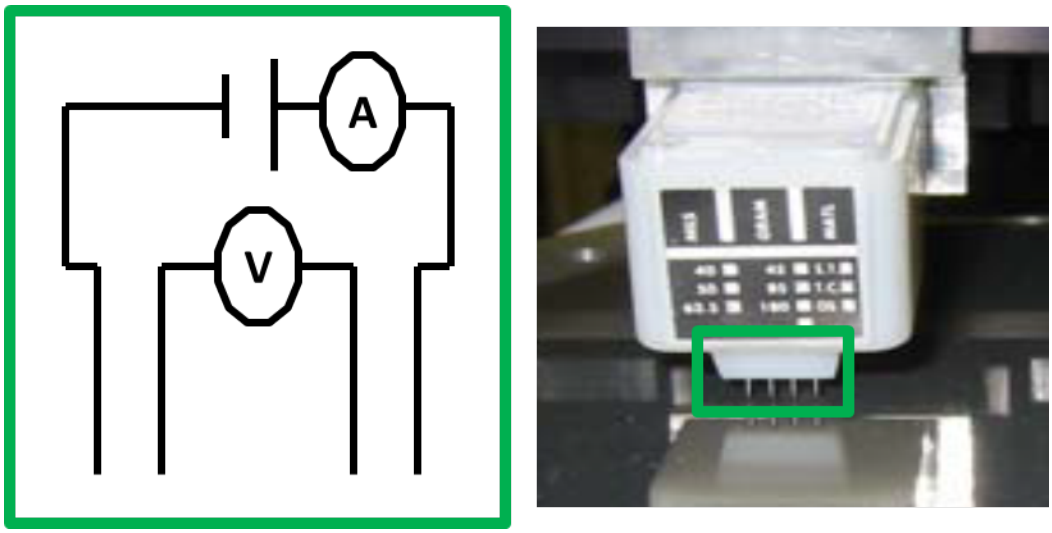

Figure 2.5 (a) Representation of current and voltage relationship as applied to a substrate. (b) Digital image of a four-point probe head with the four probes highlighted in the green box (digital image from LAMP SOP 2004).

Resistivity of a thin conductive film can be determined as follows. The resistance (R) of a rectangular block (Figure 2.6) of uniform bulk resistivity is given by equation 2.14 through 2.16.

$$R = \rho \cdot L \cdot A \quad (2.14)$$

$$A = t \cdot W \quad (2.15)$$

$$R = \rho \cdot t \cdot L \cdot W = R_s \cdot L \cdot W \quad (2.16)$$

where ρ is the resistivity of the sample, L is the length, and the area (A) is the width (W) multiplied by the height (t). The resistance (R) is therefore related to the sheet resistance (R_s) as shown in equation 2.16.

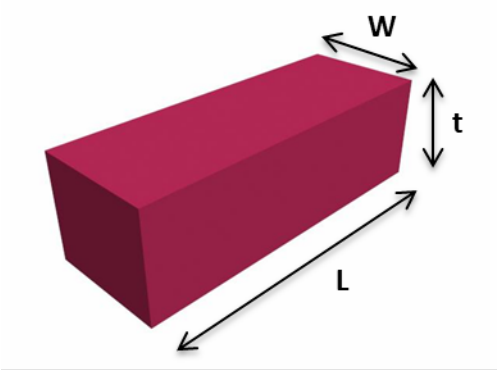

Figure 2.6 3D schematic of rectangular block exhibiting uniform resistance

The sheet resistance (R_s) is then determined by the four-point probe when a DC current is applied to the two outer probes and the voltage is measured between the two inner probes (equation 2.17). The correction factor (CF) is determined based upon the sample size.

$$Rs = VIx \text{ CF} \quad (2.17)$$

Chapter 3: MnO_2/TiN Nanotubes for Electrochemical Energy Storage

3.1 Introduction

Heterogeneous nanostructures have gained attention recently for their use in electrical energy storage systems due to the significant improvement in energy storage capabilities that arise from confining their dimensions[35,104,105] and also from the extraordinary properties realized by combining different materials. Nanostructures including nanowires[35,104,105] and nanotubes[27,33,41] provide high aspect ratio structures whose dimensions can be easily controlled and fine tuned. The combination of different materials on the nanoscale leads to synergistic properties that overcome the limiting factors of the individual materials. Energy storage systems such as electrochemical capacitors (ECCs) that rely on fast, reversible Faradaic reactions[13] have recently progressed considerably in the energy storage field due to the design and fabrication of heterogeneous nanostructures. ECCs depend on fast ion and electron transport to provide high energy density and high power density. [3,106] These superior capabilities are achieved through the short diffusion path length and the combination of favorable energy storage materials.

Recent work has shown that combining the physical properties of carbon nanotubes (chemical stability, high aspect ratio, and high activated surface area) with the energy storage ability of manganese oxide generates suitable electrodes for supercapacitor[107] and lithium battery systems.[51] Individually, the manganese oxide electrodes achieved specific capacitances of only ~36 F g^{-1}. However significant improvement was demonstrated with the addition of carbon nanotubes and Au to reach a specific capacitance of 69 F g^{-1}. Thus the synergistic behavior of heterogeneous

nanostructures enables dramatic improvements for both power and energy density. It is important to note that these measurements were made in a symmetrical cell in whcih the electrode material was the same for both the anode and cathode as opposed to a three-electrode cell or asymmetrical setup. A recent review describes the importance of reporting and determining capacitance values for electrical energy storage systems.[103]

In our previous work,[54] excellent electrochemical properties were demonstrated for electrical energy storage by combining poly(3,4- ethylenedioxythiophene) (PEDOT) with manganese oxide (MnO_2) in a coaxial nanowire structure. The PEDOT/MnO_2 coaxial nanowires, with a specific capacitance of 240 F g^{-1}, dramatically increased the specific capacitance from that of PEDOT-only nanowires with a specific capacitance of 140 F g^{-1}. The PEDOT provided significant electrical conductivity for fast electron transport and additional structural stability, while the MnO_2 provided high energy density.

Materials such as transition metal oxides, [108-110] carbon-based materials,[111] and conducting polymers[40,41] have been utilized in ECCs to provide high energy and high power density. The benefits of using MnO_2 include high energy storage capacity at a relatively low cost, natural abundance and environmental friendliness.[54] However, MnO_2 alone cannot provide superior ECC capabilities such as fast ion transport due to its low electrical conductivity and weak structural stability, especially when it is nanostructured. MnO_2 can be combined with material such as titanium nitride, which provides both high electrical conductivity (bulk material, $5x10^4$ Ω^{-1} cm^{-1})[112] for rapid electron movement and mechanical strength. TiN has been increasingly used as an electrode material[113] due to its favorable properties such as corrosion resistance, hardness (2160 kg mm^{-2}),[112] oxidative

stability and electrochemical stability. Extreme hardness provides high mechanical strength even at the nanoscale.[114,115] CNTs, like TiN, can also be combined with higher energy density materials to achieve greater capacitance.[116-118] The conductivity of CNTs greatly surpasses that of carbon nanofibers (~20–30 S cm^{-1}).[119] The specific capacitances of both TiN and CNTs are relatively low, 11.53 F g^{-1} and 17.85 F g^{-1}, respectively.[120] TiN has high electrical conductivity and can be routinely fabricated through techniques such as atomic layer deposition. The performance of CNTs, however, strongly relies on the synthesis and post-treatment methods at higher temperature.[111] These favorable properties of TiN offer a promising alternative to carbon-based materials..

In the present work, we report the synthesis of titanium nitride nanotubes (TiN NTs) surrounded by manganese oxide for use as electrochemical capacitors with superior electrical energy storage capabilities. A template-based method using an anodic aluminium oxide (AAO) porous structure and two deposition techniques, atomic layer deposition (ALD) and electrochemical deposition (ECD), are utilized to combine the favorable properties of MnO_2 and TiN into one energy storage system. The synthesis of the MnO_2/TiN nanotube arrays and the structural and electrical energy storage properties are described. The MnO_2/TiN nanotubes show high specific capacitance (834 F g^{-1} at 9 A g^{-1}) for use as a supercapacitor electrode material due to the unique design whereby the thin film of manganese oxide is in close contact with the interior and exterior of the TiN nanotubes. The large area interface between the MnO_2 and TiN optimizes performance by increasing the number of charge storage sites that occur along the surface of the active material. The increased surface area due to the removal of the template and the close proximity between MnO_2 and TiN provide enhanced charge storage capacity.

3.2 Experimental Methods

Synthesis of MnO_2/TiN Nanotubes

Titanium nitride nanotubes were synthesized by atomic layer deposition using a Beneq TFS-500 ALD reactor. Tetrakis(dimethylamino)titanium(IV) (TDMAT) and ammonia (NH_3) were used as the two precursors for the TiN baseline recipe at a base pressure of 0.7 mbar and a temperature of 175 °C. The TDMAT was pulsed for 2 s followed by 500 ms purge time. The NH_3 was pulsed for 500 ms followed by a 2 s purge time. Purging times were 500 ms and 2 s after each pulse. The TiN deposition rate was ~1.05 Å per cycle. Commercially available alumina membranes (Whatman) with pore diameter ~200 nm and pore length ~ 60 μm were used. The alumina membranes were open-ended nanopores with pore diameters of 20 nm and 200 nm on the branched and non-branched sides, respectively. The non-branched side of the alumina template was directly exposed to the ALD precursors. Gold (ca. 200 nm) was sputtered on the TiN backside using a Denton Vacuum Desktop III sputtering system. The Au backside was connected to an electrical circuit using copper tape (3M). The nanotubes were then confined to an electroactive window of 0.32 cm^2 in nominal area using Parafilm and a homemade sample holder as pictured in Figure 3.1.

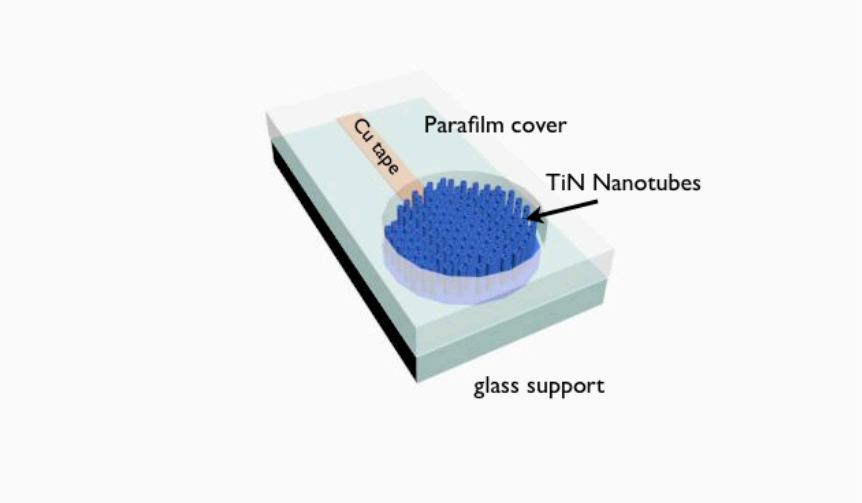

Figure 3.1 Schematic of a sample holder containing TiN nanotubes as the working electrode. The nanotubes are connected to an electrical source by copper tape. The Parafilm and glass provide a barrier so that only a confined area is exposed to the electrolyte solution.

The alumina template was removed by immersion in a 3 M NaOH solution for 60 min. After removal, the nanotubes were rinsed with deionized water. The free-standing TiN nanotubes functioned as a working electrode for further fabrication. Manganese oxide was deposited in the electroactive window at a constant potential of 0.75 V from an aqueous solution of 100 mM manganese acetate. The potential was measured versus a Ag/AgCl reference electrode and a Pt foil was used for the counter electrode. The mass of the manganese oxide deposited on the TiN nanotubes was controlled by fixing the total charge passed during electrochemical deposition.

3.3 Structural and electrical characterization

The structure of the MnO_2/TiN nanotubes was investigated using a field emission scanning electron microscope (Hitachi SU-70 SEM, operated at an acceleration voltage

of 5 keV) and a transmission electron microscope (JEOL JEM 2100 field emission transmission electron microscope (FE-TEM), 200 keV). The sample was prepared for SEM by adhering the MnO_2/TiN nanotubes on carbon tape to the SEM specimen holder. The nanotubes were prepared for TEM imaging by mechanically scratching the top surface of the nanotubes in order to release the nanotubes from the Au and TiN bottom layer. The nanotubes were released into a 6 mL solution of 1:1 water:ethanol and dried on a TEM grid.

Electrochemical studies were performed on the MnO_2/TiN nanotubes using a three-electrode system consisting of a Ag/AgCl reference electrode, a Pt foil counter electrode and Au/TiN nanotubes as the working electrode. All electrical testing was performed in 1 M $LiClO_4$ aqueous solution. Specific capacitance values were calculated using the data from the galvanostatic charge/discharge cycling between 0 and 1 V at various current densities. The mass of the MnO_2 was determined from the charge passed during electrochemical deposition and assumes 100% efficiency.

3.4 Results and discussion

Preparation of MnO_2/TiN Nanotube Arrays

The MnO_2/TiN nanotubes were prepared using atomic layer deposition (ALD) and electrochemical deposition (ECD) in the deep pores of an AAO template with a 200 nm pore diameter (Scheme 3.1). First, the TiN NTs were formed by ALD deposition of TiN into the alumina membrane with a pore diameter size of 200 nm and a pore length of ~60 μm. A 100 nm of TiN was deposited into the pores in order to fill the pore opening to achieve a continuous electrical contact of TiN. ALD deposited TiN penetrated conformally to a depth of ~5 μm into the AAO porous structure, forming a thin film

along the walls of the AAO. With a fixed pore depth and diameter of TiN filling the pores, the resulting TiN nanotube dimensions were kept constant for this study. The deposition depth of ALD TiN can typically go up to an aspect ratio of around 170,[90] that is about 30 µm depth with a 200 nm diameter cylindrical pore. However, in this study, a commercial Beneq system was used whereby the penetration depth is drastically decreased.

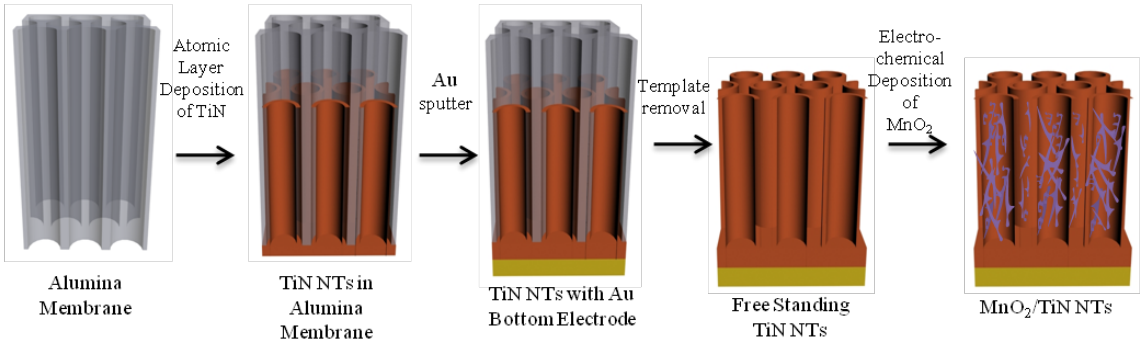

Scheme 3.1 Synthesis of MnO_2/TiN nanotubes. (1) Atomic layer deposition of 100 nm into AAO pores, (2) 200 nm Au sputtered on a TiN film, (3) removal of the AAO template using 3 M NaOH, and (4) electrochemical deposition of MnO_2 along the TiN nanotubes.

Resistivity measurements were performed with a four-point probe in order to observe any changes in the conductivity of TiN on planar substrates. We found that the TiN resistivity remained of the same magnitude (~100 mΩ cm), which confirms that TiN provides relatively good conductivity on a planar substrate. Table 3.1 shows results from four-point probe measurements of TiN on two substrates, Al and ITO on glass.

Substrate	TiN Thickness (nm)	Conductivity (S cm^{-1})
Aluminum	50	131
ITO/glass	50	140

Table 3.1 Conductivity measurements obtained for TiN using a four-point probe.

After conformal deposition into the pores to produce the TiN NTs, a thin layer (200 nm) of Au was sputtered on the backside of the AAO template containing the TiN nanotubes for additional mechanical support. Figure 3.2 shows an SEM of the bottom-side of TiN nanotubes after removal of the alumina template and without Au sputtering. Here it is visible that the bottom surface of TiN has a somewhat curved structure due to the nature of the porous template. The addition of a bulk Au bottom layer added additional structural support.

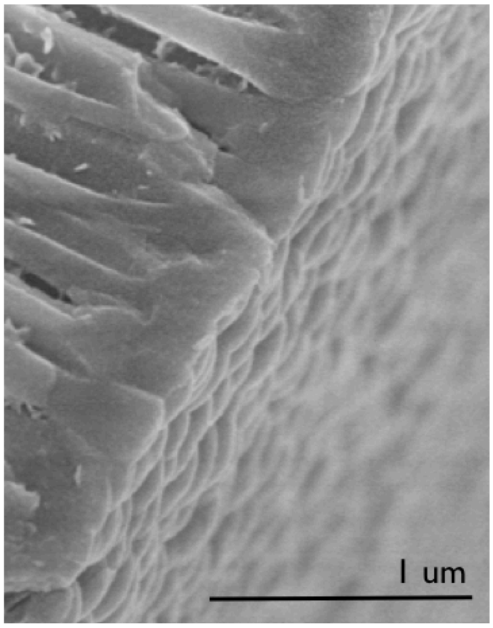

Figure 3.2 SEM image of the bottom side of TiN nanotubes after removal of the alumina template. The curved structure was covered with a layer of sputtered Au (~200 nm) for additional mechanical support.

After sputtering, the AAO template was removed using a 3 M NaOH solution to expose most of the surface area of the TiN NTs. This critical removal step allowed for both the inside and outside surfaces of the TiN NTs to be exposed to the electrolyte solution for ECD of MnO_2 and later to the electrolyte for electrochemical evaluation. Figure 3.3 shows the stand-alone TiN NTs prior to electrochemical deposition of MnO_2.

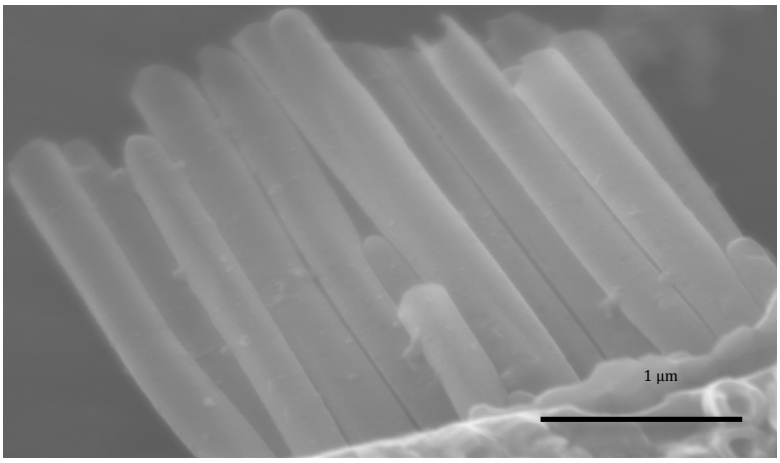

Figure 3.3 SEM image of an array of stand-alone TiN nanotubes without MnO_2.

MnO_2 was deposited electrochemically along the interior and exterior TiN surfaces. A three-electrode cell was used for ECD of MnO_2 with an Ag/AgCl reference electrode, a platinum counter electrode, and the TiN nanotubes as the working electrode. The amount of MnO_2 deposited was controlled by the integrated charge passed during the deposition. Electrochemical performance testing indicated that 25 mC of MnO_2 (see below) achieved the highest specific capacitance. Deposition was performed at a voltage of 0.75 V in a 100 mM solution of manganese acetate. The MnO_2/TiN nanotubes were then structurally and electrically characterized for their use in electrochemical energy storage.

Electron Microscopy

Electron microscopy was used to characterize the MnO_2/TiN nanotubes to observe the full nanostructure design. Figure 3.4a shows a top view SEM image of the MnO_2/TiN nanotube array. The MnO_2/TiN nanotubes are ~200 nm in diameter. The average length of the tubes is ~5 μm. Figure 3.4b shows a side view of the MnO_2/TiN nanotubes. MnO_2 can be observed on both the inner and outer surfaces of the TiN nanotubes. Figure 3.4c shows a partial TEM image of an MnO_2/TiN nanotube. The bottom of Figure 3.4c represents the top of the nanotube. Figure 3.4d shows a magnified TEM image of the nanotube in Figure 3.4c. One can see an MnO_2 film both within the nanotube and on the outer surface of the nanotube. A corresponding TEM image is given in Figure 3.5a. Elemental analysis was performed with EDS on the MnO_2/TiN nanotubes in order to confirm and locate the titanium and manganese oxide films. Figures 3.5b and c show EDS line scans of the corresponding nanotube (Figure 3.5a) for titanium (Figure 3.5b) and manganese (Figure 3.5c). In Figures 3.5c and e, one can see that the manganese film is located on both the inner and outer sides of the nanotube as expected for nominally round nested nanotubes.[99] Figure 3.5e illustrates more clearly the distribution of Mn along the TiN nanotube wall. The EDS images in Figure 3.5d are consistent with the EDS line scans above. The MnO_2/TiN nanotubes were observed with high resolution-TEM (HR-TEM) for further structural characterization. HR-TEM imaging as shown in Figure 3.6a and b of the MnO_2/TiN nanotubes showed the amorphous structure of both the TiN and MnO_2 materials. Figure 3.7 also depicts the presence of MnO_2 on both the inner and outer walls of the TiN nanotube. Additional EDS data are provided in Figures

3.8a and b, which shows the spectrum of elements with the coordinating elements' atomic and weight percent.

For further chemical confirmation Raman spectroscopy and x-ray diffraction (XRD) were used to analyze the heterogeneous nanostructure. The results are described in the Appendices A.2 and A.3.

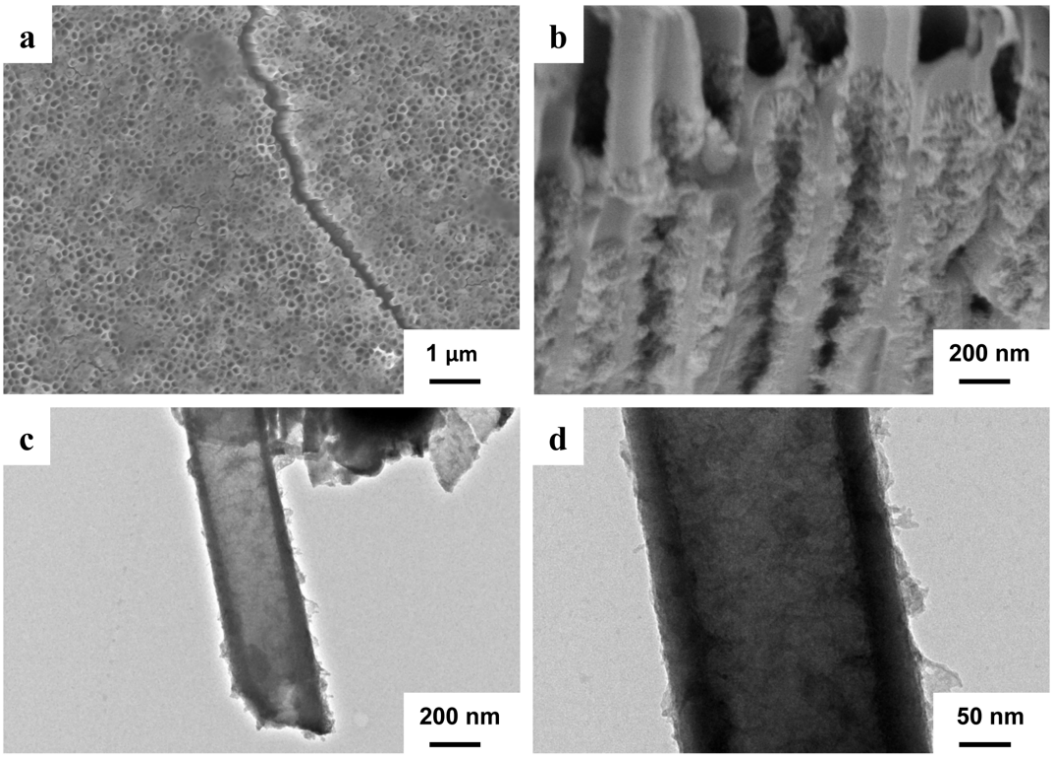

Figure 3.4 (a) SEM top view and (b) side view of MnO_2/TiN nanotubes. (c) TEM image of a singular MnO_2/TiN nanotube whereby the bottom of the image represents the top of the nanotube. (d) Higher magnification version of the TEM image in (c).

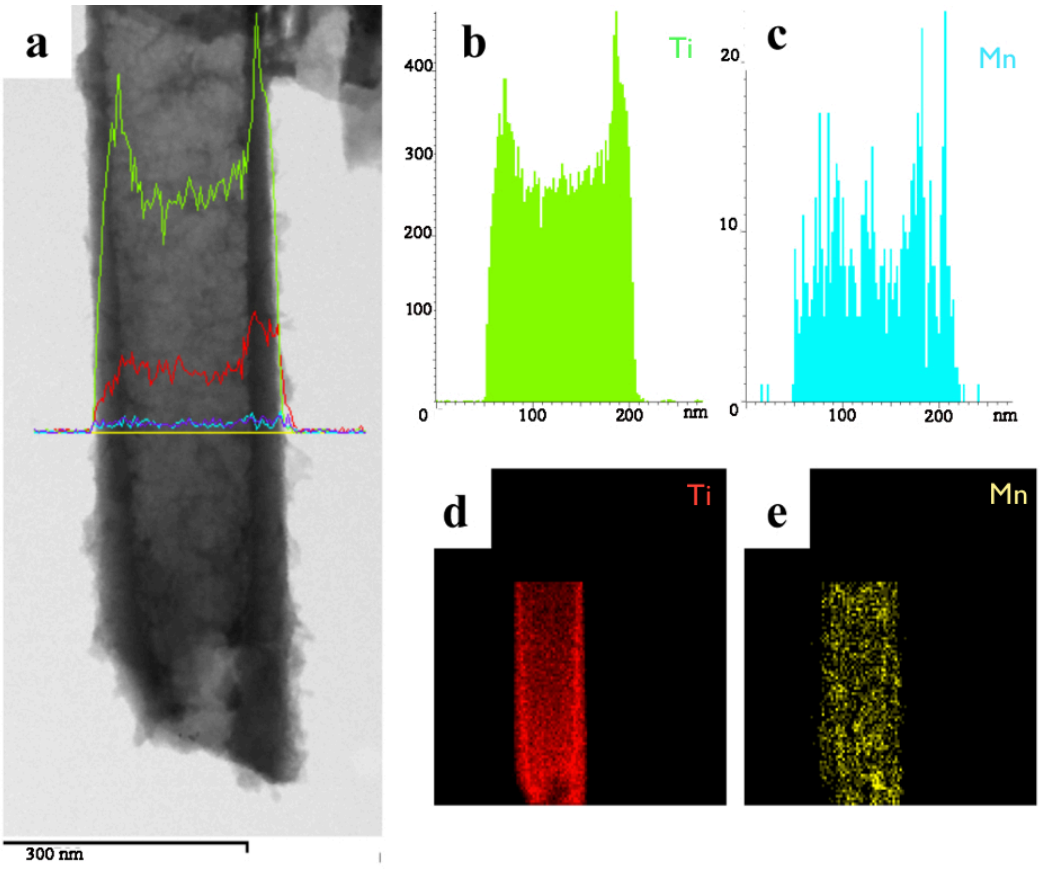

Figure 3.5 (a) TEM Image of a single MnO_2/TiN nanotube. EDS line scan of (b) titanium (c) manganese and EDS mapping of (d) titanium and (e) manganese.

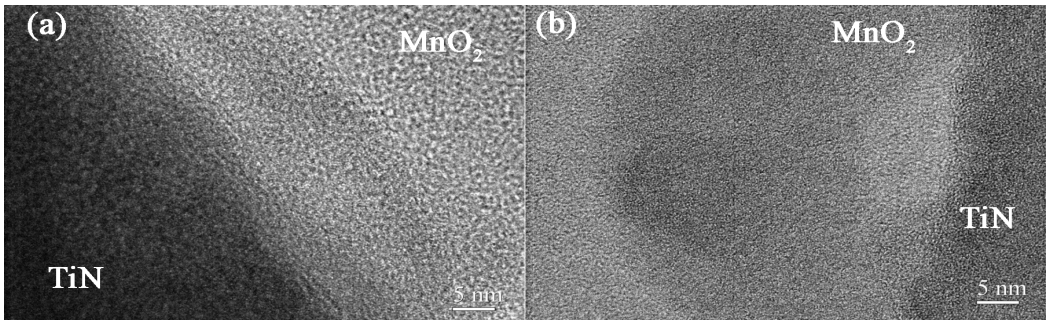

Figure 3.6 (a,b) HR-TEM images of the MnO_2/TiN nanotube nanostructures. The images show the amorphous material of both MnO_2 and TiN.

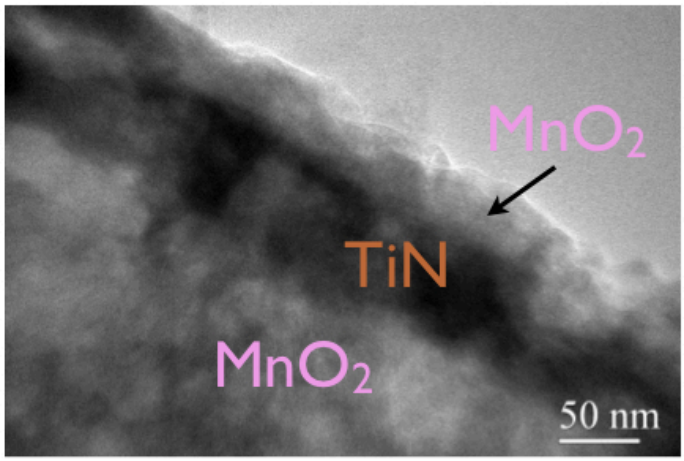

Figure 3.7 TEM image of the edge of the MnO_2/TiN nanotubes

(a)

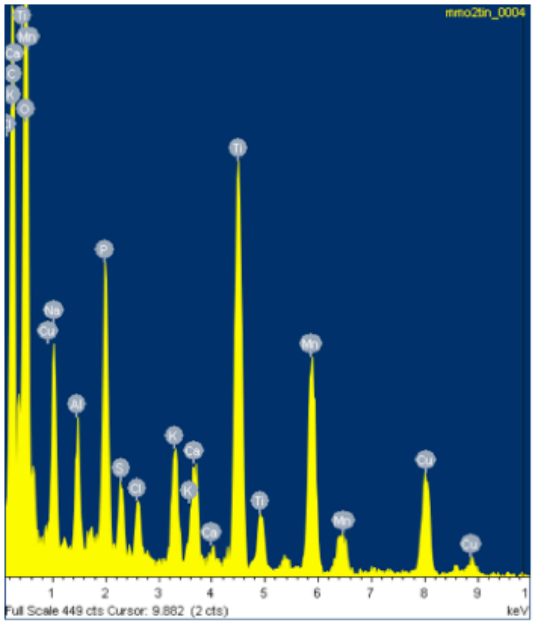

(b)

Element	Weight %	Atomic %
C	20.25	32.96
O	**35.84**	**43.78**
Na	5.56	4.78
Al	2.61	1.89
P	6.57	4.14
S	1.76	1.07
Cl	1.35	0.75
K	2.99	1.49
Ca	2.49	1.21
Ti	**12.61**	**5.14**
Mn	**7.98**	**2.84**
Total	100	

Figure 3.8 EDS analysis of MnO_2/TiN nanotubes showing (a) spectrum of elements and (b) corresponding weight and atomic percentage, highlighting the elements of interest in green/bold.

Optimization of Electrochemical Deposition

The deposition parameters were varied for ECD of MnO_2 on the TiN surface in order to optimize the electrochemical performance of the nanotubes. By controlling the charge passed during deposition, we were able to control the distribution of MnO_2 along the surface of the TiN nanotubes and minimize the amount deposited at the pore entrances. Excessive amounts of MnO_2 deposited resulted in large masses of MnO_2 concentrated on the top surface of the TiN nanotubes. Figure 3.9 shows an SEM image of the TiN nanotubes coated with a thick layer of MnO_2. We explored a variety of deposition parameters including deposition of MnO_2 by cyclic voltammetry, as well as adjusting the electrolyte solution to manganese sulfate. These methods, however, did not prove to be successful. We discovered that by controlling the charge (mC) during the electrochemical deposition of MnO_2 we were able to successfully deposit a thin conformal layer of MnO_2 along the inner and outer surfaces of the TiN nanotubes i.e. uniform MnO_2 thickness along the nanotube. This controlled deposition allows not only close contact between MnO_2 with TiN along the inner and outer surface of the TiN nanotubes, i.e. uniform MnO_2 thickness along the nanotube, which enhances electron transport due to the high electrical conductivity of TiN, but also assures uniform ion diffusion times into the MnO_2 material. We found that successful and uniform deposition into the pores occurred during depositions in which 15–25 mC were passed (Figure 3.10).

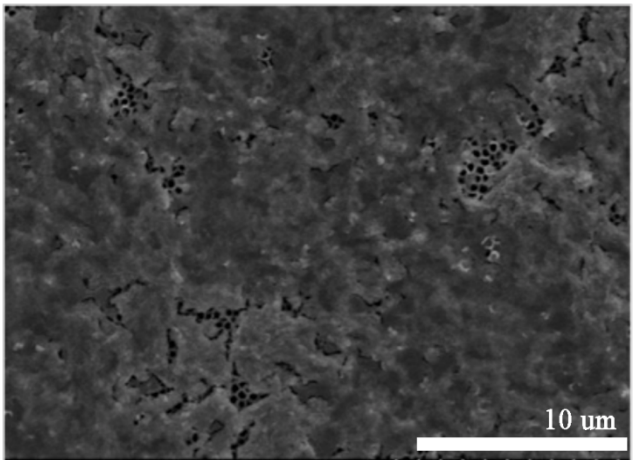

Figure 3.9 SEM top view image of excessive MnO_2 deposited onto the TiN nanotubes. We believe that when this result occurs the capacitance capabilities of the system are limited as the MnO_2 does not reach into the TiN nanotubes. In this situation we are unable to benefit fully from the high conductivity and mechanical strength of TiN.

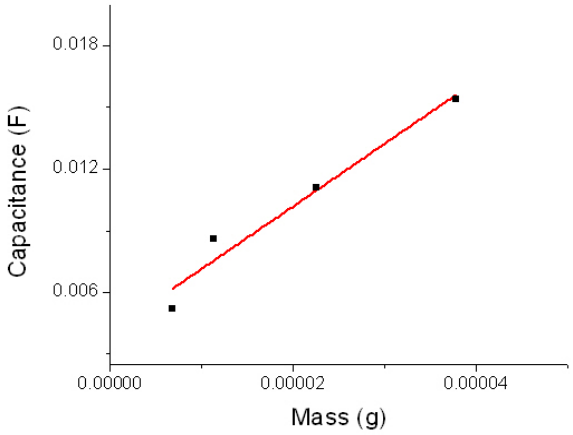

Figure 3.10 Linear fit (red line) of capacitance versus mass of MnO_2 deposited onto the TiN nanotubes (black dots). We found that the capacitance results varied for a given amount of MnO_2 deposited.

Cyclic Voltammetry and Galvanostatic Charging/discharging Characterizations

Electrical characterization of the MnO_2/TiN nanotubes was performed using CV and GV charge/discharge cycling curves. Figure 3.11a shows the comparison of TiN-only nanotubes (black line) and MnO_2/TiN nanotubes (red line) at a scan rate of 100 mV s^{-1}. Clearly it is the MnO_2 that supplies charge storage functionality, as expected. Figure 3.11b shows the resulting CV curves of the MnO_2/TiN nanotubes in a 1 M $LiClO_4$ aqueous electrolyte solution. All CV scans were performed in a potential range of 0–1 V at scan rates of 50, 100, 250, 500, and 1000 mV s^{-1}. The MnO_2/TiN nanotubes showed scaling behavior in current as the scan rate was increased. The rectangular shape that indicates near ideal capacitive property, however, is slightly distorted at higher scan rates.

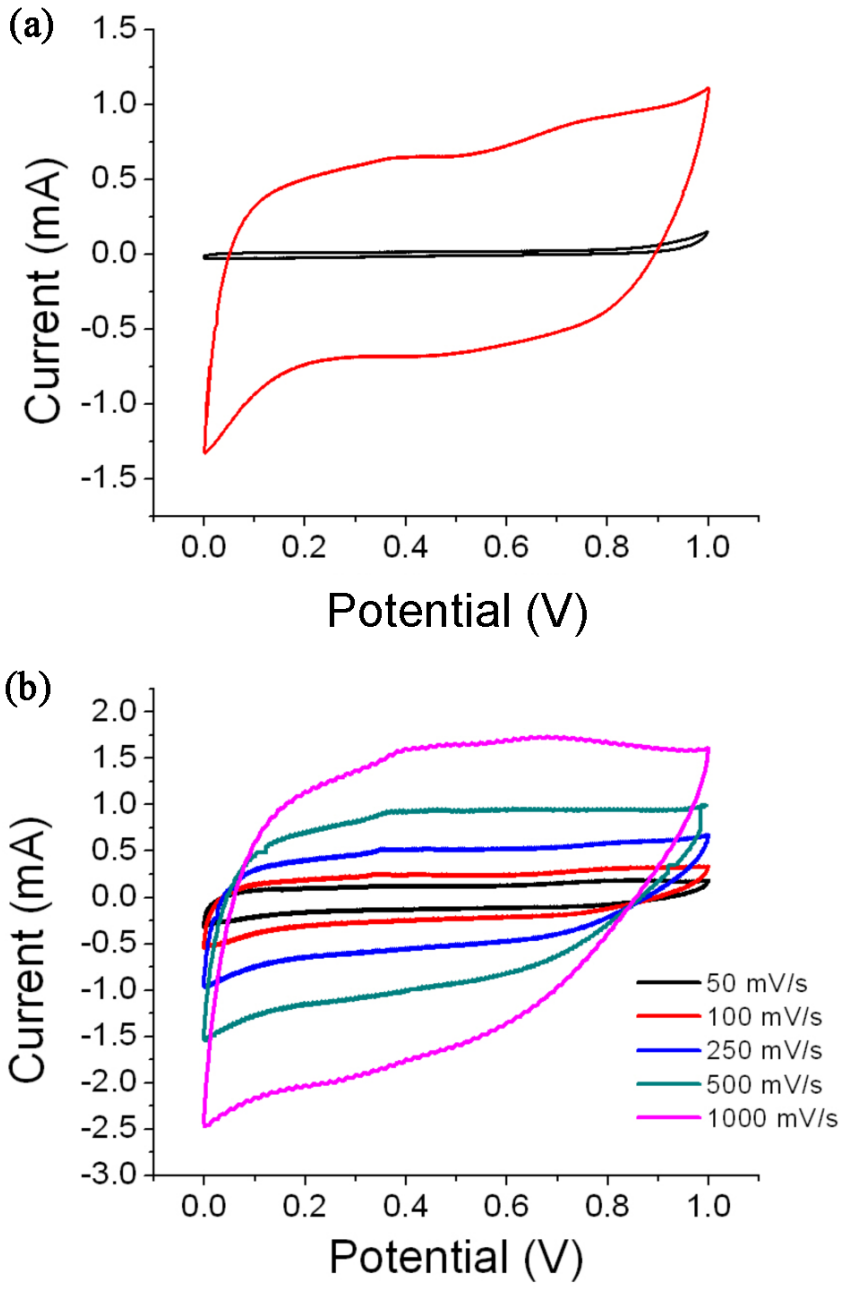

Figure 3.11 (a) Cyclic voltammetry of TiN nanotubes (black) and MnO_2/TiN nanotubes (red) from 0-1 V in 1 M $LiClO_4$ aqeuous solution at a scan rate of 100 mV s^{-1}. (b) Cyclic voltammetry of MnO_2/TiN nanotubes in the potential range from 0-1 V at increasing scan rates of 50, 100, 250, 500, 1000 mV s^{-1} (black, purple).

The electrochemical stability of the MnO_2/TiN nanotubes was also studied by using GV cycling curves (Figure 3.12) obtained from charging and discharging the nanotubes from 0 to 1 V in a 1 M $LiClO_4$ aqueous solution for 350 cycles at a specific current of 9 A g^{-1}. The cyclability of the MnO_2/TiN nanotubes is somewhat promising, however, in Figure 3.12a there is a significant initial drop in symmetry from the second to fiftieth cycle. Interestingly, the time for charging during the second cycle is slightly longer than the time for discharging. For the fiftieth and greater cycles, however, the reverse seems to hold, i.e. the discharging time is longer than the charging time. This scenario in the second cycle is likely due to an irreversible oxidation reaction, which is possibly associated with oxidation of titanium. X-ray photoelectron spectroscopy (XPS) was used to analyze the ALD TiN film and showed that even prior to electrical testing TiN has a tendency to form a thin oxide layer on the surface (Appendix A.4). Figure 3.12b shows the specific capacitance results from cycling the nanotubes at a specific current of 15 Ag^{-1} over 350 cycles.

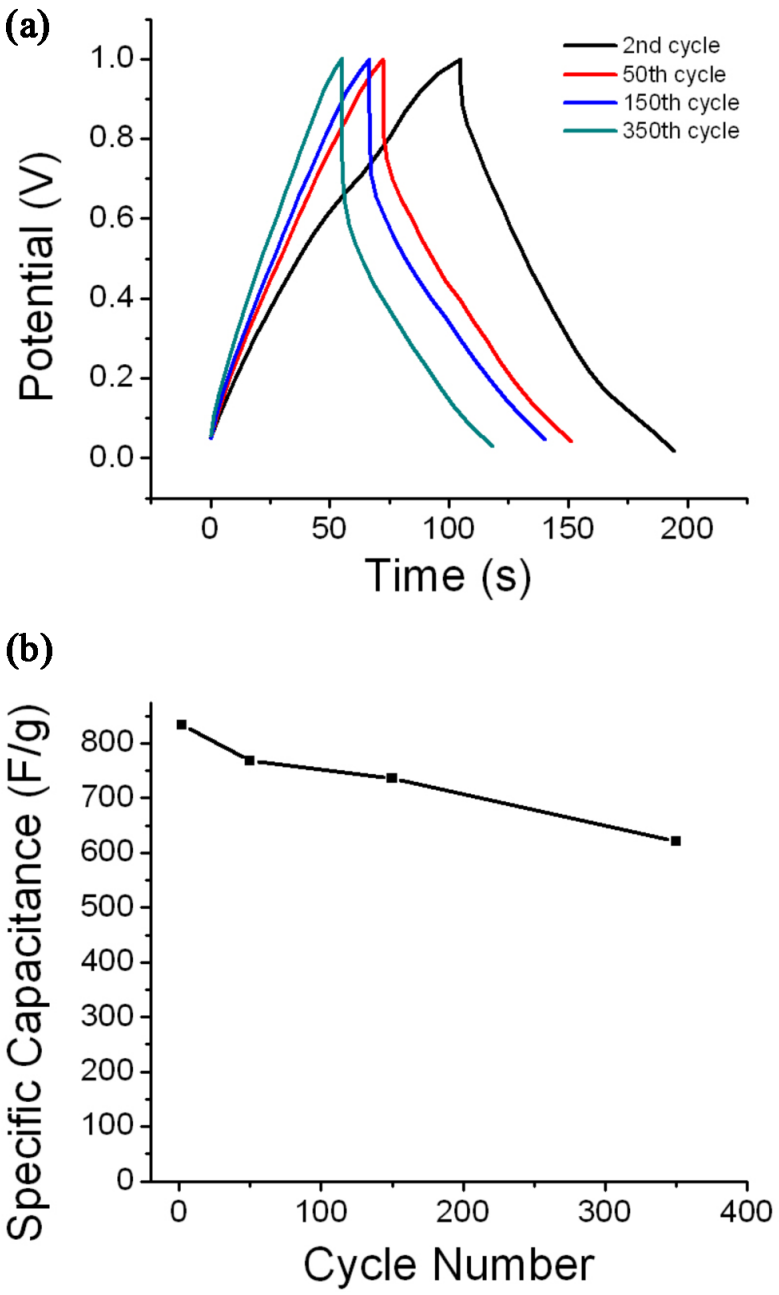

Figure 3.12 (a) Galvanostatic charging and discharging cycling of the MnO_2/TiN nanotubes between 0 and 1 V (vs. Ag/AgCl) at a specific current of 9 A g^{-1} for the second cycle, 50th cycle, 150th cycle, and 350th cycle in 1 M $LiClO_4$ aqueous solution. (b) Specific capacitance versus cycle number at 15 A g^{-1} from GV cycling up to 350 cycles.

We believe that the decrease in specific capacitance after hundreds of cycles may be due in part to damage of the TiN nanotubes at the very top of the structure. The thickness of TiN, deposited by self-limiting atomic layer deposition into the pores is between 5–10 nm at the pore tip, which may be too thin to withstand continuous cycling at higher current densities. Figure 3.13 shows the TiN nanotube tips after 1000 GV cycles at 9 A g^{-1}. There is visible cracking on the top of the TiN nanotubes, possibly due to the thin nature of the TiN at the pore tops.

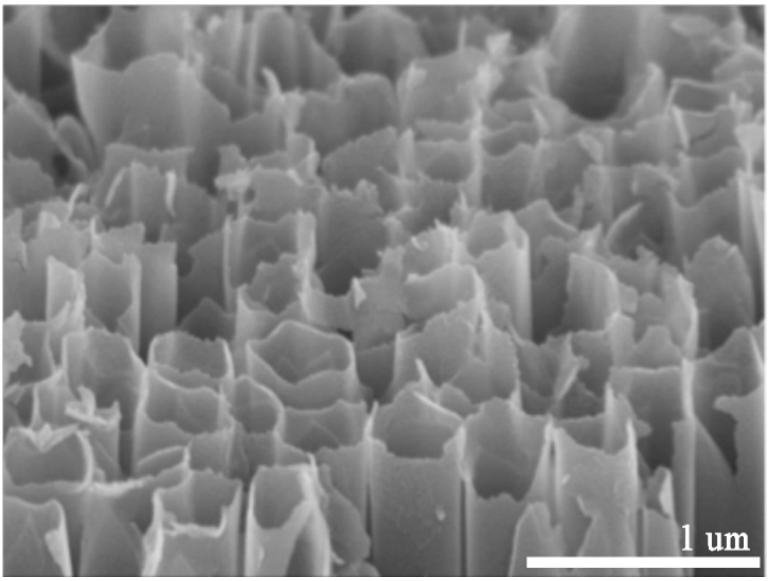

Figure 3.13 SEM top view image of TiN nanotubes after GV cycling at 9 A g^{-1} for 1000 cycles. This image illustrates the thin nature of the TiN nanotubes at the top and the cracking that occurs as a result of higher current densities. The cracking of the TiN nanotubes may lead to the loss of specific capacitance.

MnO_2/TiN nanotubes were cycled 1000 times from 0-1 V at 18 A g^{-1}. During the initial 200 cycles there is a drastic decrease in specific capacitance, as shown in Figure 3.14.

After 1000 cycles, the specific capacitance of the MnO_2/TiN nanotubes is still well above that of regularly nanostructured MnO_2.

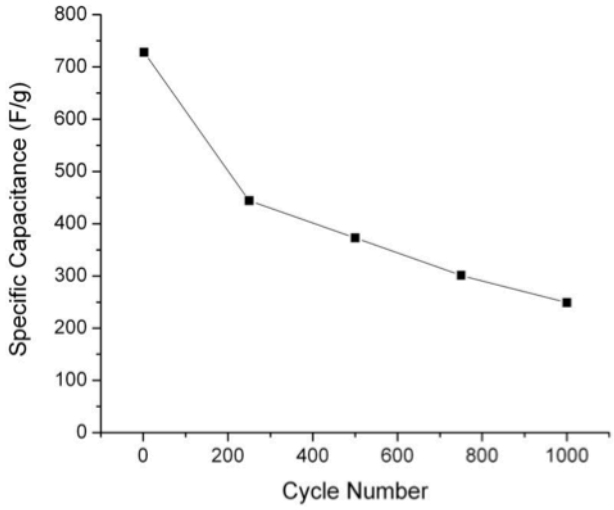

Figure 3.14 Specific capacitance measured during GV cycling of MnO_2/TiN nanotubes over 1000 cycles from 0-1 V at 18 A g^{-1}in 1 M $LiClO_4$ aqueous solution.

Determination of Specific Capacitance

Specific capacitance was determined based on GV results. We achieved a specific capacitance of 662 F g^{-1} for the MnO_2/TiN nanotubes at a specific current of 45 A g^{-1}. This value was based on the mass of the manganese oxide material alone as determined from the charge passed during deposition. The results in Figure 3.15 show the specific capacitance values versus specific current for the average of three separate MnO_2/TiN nanotube arrayed structures when using the MnO_2 mass only (black) and when the mass of TiN and MnO_2 were used (red) to calculate specific capacitance. We believe that both of these numbers are essential to studying this material for energy storage systems. The

specific capacitance calculated with only the MnO_2 material is a valuable number given that the MnO_2 is the only material directly involved with charge storage and shows the intrinsintrinsinsintrintrinsic properties of MnO_2. Calculated values for volumetric and intrinsic properties of MnO2. The calculated values for volumetric and footprint-normalized capacitances were 46.6 F cm^{-3} and 23 mF cm^{-2}, respectively. All of these values should be considered when addressing the system as a whole and for potential applications as electrode material in energy storage systems. The resulting specific capacitances are very promising for energy storage technologies.

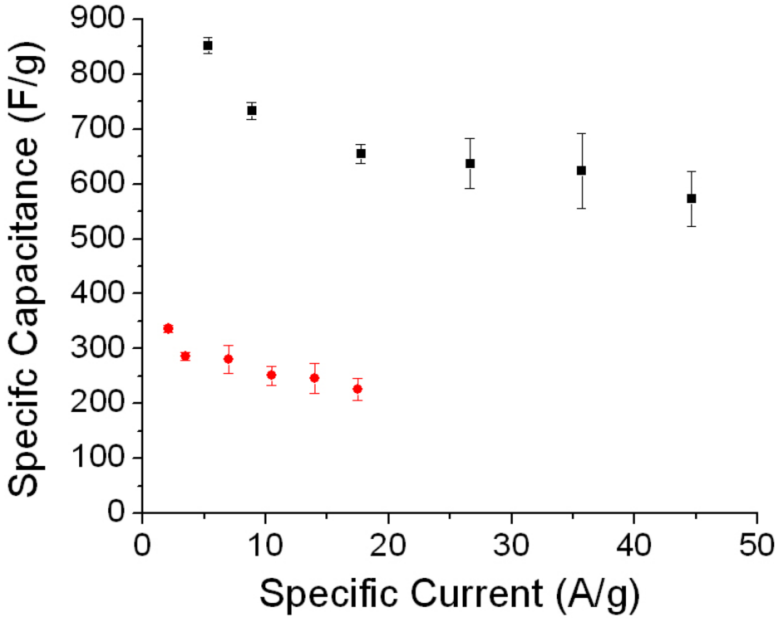

Figure 3.15 The average specific capacitance values for three individual MnO_2/TiN nanotube arrays at increasing specific current (Ag^{-1}) calculated with MnO_2 mass alone (black) and MnO_2 and TiN mass combined (red).

Comparison of MnO2's Contribution to Specific Capacitance

MnO_2/TiN nanotubes are directly compared with other nanocomposite studies previously performed in our laboratory with heterogeneous nanostructures in Table 3.2. A variety of morphologies and compositions have been demonstrated with MnO_2 as one of the principal energy storage materials plus an additional material to potentially provide synergistic effects. Based on the results for heterogeneous nanostructures presented below, it can be seen that MnO_2 out performs its pure counterpart.

Composite	**Method of Synthesis**	**Current Density (A/g)**	**Pure Counterpart (F/g)**	**Composite Specific Capacitance (F/g)**	**MnO_2's Contribution (F/g)**
Coaxial MnO_2/PEDOT NWs[54]	ECD	5	210 MnO_2 Nanowires	270	300
MnO_2 Nanocrystals in PEDOT[55]	ECD and Chemical Synthesis	5	110 PEDOT Nanowires	250	410
MnO_2/$Ni(OH)_2$ Nanowires	ECD	5	210 MnO_2 Nanowires	1230	650
MnO_2/TiN Nanotubes[63]	ALD and ECD	7	120 MnO_2 Thin Film	266	673

Table 3.2 Heterogeneous nanostructured composites in which MnO_2 is one of the main energy storage materials are compared. Specific capacitance is calculated for the nanocomposites and the contribution to specific capacitance from MnO_2 are calculated. (Adopted from EFRC, J. Duay 2012)

Figure 3.16 illustrates the specific capacitance attributed to MnO_2 for a variety of heterogeneous nanostructures. The orange text specifies the pure counterpart in the nanocomposite. The MnO_2 thin film, with the greatest specific capacitance, further confirms that MnO_2 outperforms its pure counterpart.

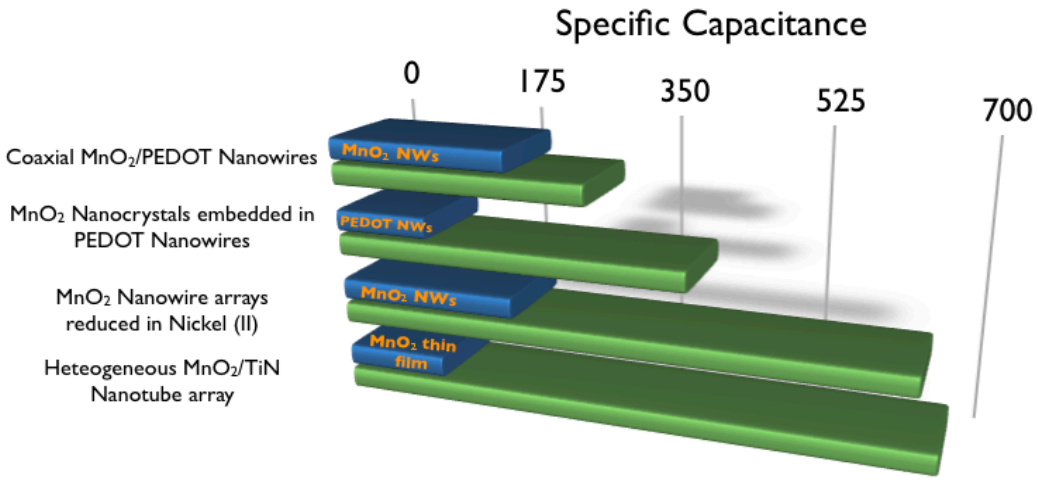

Figure 3.16 Nanostructures are compared by the specific capacitance attributed to MnO_2. Inserted description represents the pure counterpart. (Adopted from EFRC, J. Duay 2012)

3.5 Conclusions

In summary, we have described the fabrication of MnO_2/TiN nanotubes that utilize the high surface area of both the inner and outer surfaces of the TiN nanotubes. We combined two facile deposition techniques, atomic layer deposition and electrochemical deposition, into an AAO template, demonstrating high-precision methods for engineering heterogeneous nanostructures as well as substantial potential for future system designs. The close proximity of the nanomaterials facilitates fast charging and discharging as a supercapacitor. The superior results shown by combining an energy

storage material such as MnO_2 with a highly conductive and mechanically stable material such as TiN demonstrates a promising nanostructured electrode design for electrochemical energy storage systems.

Chapter 4: AAO Template Design for the Synthesis of 3D Heterogeneous Nanostructured Electrodes

4.1 Introduction

Current research in electrical energy storage technology is focused on the ability to increase energy density without sacrificing power density. Energy storage systems such as batteries and capacitors are well-studied, mature technologies [4,57] and in order to obtain the notable increase in both energy and power density necessary to store and deliver energy on demand, there is a need for a more drastic change in the approach to advancing electrical energy storage technology. Many scientists now believe the answer to generating such technologies lies in the use of multi-dimensional electrical energy storage materials, specifically three-dimensional (3D) electrode materials. In addition to the small footprint of 3D nanostructured electrodes, an electrical energy storage system would benefit from the short transport lengths for ions within the electrode as well as between the anode and the cathode.[42]

3D nanostructures provide several anticipated solutions to problems that arise in one-dimensional (1D) electrode materials. For example, when 1D nanostructures are fabricated with extremely high aspect ratios, they tend to have high electrical resistance as well as weakened structural stability. Long 1D nanostructures also have a tendency to aggregate. 3D electrode materials, on the other hand, provide a continuous electron pathway due to the interconnectivity of the electrode material (Figure 4.1). Due to the physical nature of interconnecting channels, the material can exhibit structural robustness similar to that of its bulk counterpart.[4] An additional benefit is that the electrolyte can penetrate and contact the electrode material through the interconnected pores.

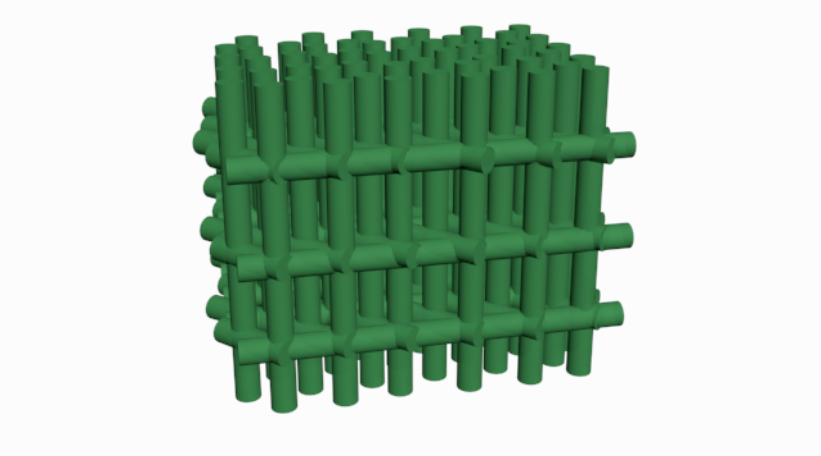

Figure 4.1 Schematic of a proposed 3D nanostructured electrode

One major focus in advancing electrical energy storage technology is on the design and fabrication of supercapacitors to help bridge the gap between high-energy-density batteries and high power density capacitors. The fundamental charge-storage of supercapacitors occurs at or within close proximity of the electrode/electrolyte interface and therefore 3D nanostructures offer potentially substantial improvements to both power and energy densities.[4] These nanoarchitectures will likely enhance the electrical and ionic interactions within the supercapacitor. The 3D approach to electrical energy storage is at an early stage and therefore there exist several challenges in the design, fabrication, characterization and understanding of 3D nanostructures. For example, many of the characterization challenges lie in the understanding of the contribution of the surface due to the large surface-to-volume ratios and the fact that the area of interest can lie below the surface. Many of the recently reported 3D nanostructures are of a disordered nature making it more of a challenge to understand the interparticle interactions and the major components of the system. One goal for the future design of 3D nanostructures is to optimize the pore size and order. Controlling these parameters could aid in the

advancement of technology in order to achieve optimal electrochemical performance and provide more straightforward analysis of 3D nanoarchitectures.[42]

Much of the attention to the development of 3D structures has focused on using appropriate nanoscale building blocks as well as on strategic use of the void space. One of the critical approaches to constructing 3D nanostructures is exploiting self-limiting reactions to generate ultrathin conformal films or coatings.[4] A well-controlled, interconnected pore structure will facilitate solvent infiltration and ion transport and will benefit from product mass transport. Well-defined structures will also help with the understanding of correlations between the structure and its properties. Currently, self-limiting techniques for the fabrication of electrode materials include layer-by-layer,[121] self-assembly,[122] atomic layer deposition (ALD),[123] and electrochemical deposition (ECD)[89,124] processes.

ALD is an ideal self-limiting deposition technique for use in 3D nanostructures due to the surface confined reactions and termination of the top surface layer chemistry, restricting growth to a single monolayer.[125] The ability of ALD to deposit thin, conformal films within high-aspect-ratio nanostructures has been demonstrated. [90,91] Such deposition of thin films is therefore an ideal technique for 3D nanostructures. There are currently many electrical energy storage materials available to modify 3D nanostructures such as RuO_2, TiO_2, TiN, MnO_2, V_2O_5. ALD has been used to coat 3D nanostructures including aerogels of carbons,[93] silica,[126] polymer templates,[92] and AAO.[127]

ECD of polymers and electropolymerization are alternative deposition technique for the development of precise 3D nanostructures. Electropolymerized materials are flexible films and can be deposited as conformal ultrathin thicknesses (~10-100 nm).

Long *et al*.[128] reported the deposition of a protective polymer coating to stabilize MnO_2 ambigels in aqueous acid. The self-limiting deposition of o-phenylenediamine allowed for a conformal, nanoscale network of polymer material and acted as a barrier to acidic electrolyte. Wang *et al*.[129] reported the addition of ordered whisker-like polyaniline (PANI) on the surface of mesoporous carbon. The 3D composite structure of PANI/mesoporous carbon showed a high specific capacitance of 900 F g^{-1} at 0.5 A g^{-1}.

3D nanostructured networks are quickly becoming a popular focus of research for their potential use in electrical energy storage applications. Much of the research completed thus far includes the design and fabrication of complex hierarchical heterogeneous nanostructures,[130] ordered mesoporous materials,[131] and disordered porous 3D nanostructures.[132] These designs have many advantages, including assembly from lower level nanoscaled building blocks, high conductivity, interconnected pore structure, and high pore volume. One of the most promising examples of 3D nanostructures is the synthesis of 3D aperiodic hierarchical porous graphitic carbon as a potential electrode for supercapacitors. Wang *et al*.[21] reported the synthesis of 3D networks of nanoparticles with a core of macropores that acted as ion-buffering reservoirs, to increase ion conductivity, and micropores to enhance electronic conductivity while also increasing the electric double layer. This design showed high energy density even at high charge/discharge rates.

One of the disadvantages to these complex structures is the understanding of key ionic and electronic interactions. Due to the disordered porous network or complex design, it is often difficult to understand fully the important interactions during the charge storage process. Controllability will also become an important parameter for the design

of 3D interconnected networks. A recent review[42] proposed the design of future 3D template-based nanostructures for advanced electrical energy storage capabilities. This design allows for precise control over both pore size and order for the interconnected nanonetwork. Controlling these parameters could potentially lead to optimal electrochemical performance. One way in which to control these parameters is the use of a well-ordered nanostructured template. AAO has provided a self-organized, highly ordered nanostructured template for the development of high precision nanostructures for a variety of applications. Pore dimensions and spacing are well controlled based on basic electrochemical techniques. The AAO template has been shown tobe able to attain a greater diversity of structures based on the manipulation of such electrochemical parameters to form branched alumina templates, as discussed in Chapter 1. These examples demonstrate the versatility of AAO for constructing well-defined nanoporous structures.

It has been well documented that the pore diameter of AAO is linearly proportional to the anodizing voltage and the diameter attributed by the anodization can be expressed as:

$$D_p = \lambda_p \cdot U \qquad (2.5)$$

where the pore diameter (D_p) is equal to the anodizing voltage (U) and λ_p represents a proportionality constant of approximately 1.29 nm V^{-1}.[72] The Y-branched structures previously mentioned were based on an adjustment to the anodization voltage of $1/\sqrt{n}$. The reduction in voltage by a factor of $1/\sqrt{n}$ resulted in a Y structure at the site of pore growth. Tien *et al*.[77] also found that if the voltage is reduced slowly, the stem pores

divide branch pores gradually (i.e. at several depths), but if the voltage is divided abruptly it leads to a sharp interface.[78]

Another key component of the AAO structure is the presence of the barrier layer located at the pore bottom. This oxide layer separates the inner nanopore space and the bottom aluminum layer, as discussed in Chapter 2. The structure and composition of the barrier layer have been well studied.[133,134] Wood and O'Sullivan[72,133] first suggested that reducing the anodization potential would result in barrier layer thinning due to a field-assisted dissolution of the oxide. Studies showed that a progressive reduction of the anodizing potential leads to a thinning of the barrier layer and eventually to its perforation.[58] Gosele *et al*.[135] further demonstrated how the thinning of the barrier layer provided access to the bottom Al substrate for further modification. Nickel was electrochemically deposited within the nanoporous structure using the bottom Al substrate for electrical contact.

In this work, we demonstrate the design and fabrication of highly controlled 3D AAO template-based nanostructures for potential use in electrical energy storage applications. An AAO template is used for high precision fabrication of an interconnecting network of nanopores. By ramping the anodization voltage in a step-wise manner to the 'disordering' regime for AAO pore growth, branched pores are initiated and controlled for slightly lateral growth of new pore channels. Using a basic chemical etching process, parallel nanopores are connected at specific regions along the original nanopore structure. The complete nanostructure consists of vertical well-organized nanopores with cross-pore connections allowing access for further modifications. By repeating the voltage drop and rise technique, we illustrate the ability

to create multiple connections between nanopores at desired positions. Deposition techniques such as atomic layer deposition and chemical synthesis are used to demonstrate the construction of interconnecting channels. After removal of the 3D alumina template, creation of a stand-alone network of ordered dimensions is accomplished. Further studies demonstrate high control of the AAO pore structure through a slightly different voltage ramping technique. In this process, the voltage is continuously ramped down at an ideal rate to reduce the thickness of the barrier layer. After thinning of the barrier layer, a chemical etching process is employed to provide access to the bottom Al layer. The two different ramping techniques are discussed and their potential for being used collectively for the design of 3D nanostructures is proposed.

4.2 Experimental Setup

An anodic aluminum oxide (AAO) template was fabricated using a two-step anodization process. Briefly, a high purity Al foil (99.99%) was degreased and electropolished using 5:1 ethanol:perchloic acid. The first anodization took place in a 0.3 M oxalic acid electrolyte at 40 V for seven hours. The electrolyte temperature was maintained at 8° C. During anodization the Al foil was placed in a sample holder to expose just one side to the electrolyte solution. The Al foil was then etched using a phosphoric acid/chromic acid solution at 60° C. The second anodization voltage and time were varied for different samples (see below). The anodization process was completed using a Keithley 2400 power source controlled by National Instruments' LabView software (Appendix A.6), where the anodization voltage was controlled at a desired ramping rate. A pore-widening (chemical etch) step took place at the conclusion of the second anodization in a 5% wt. phosphoric acid solution at 38° C.

Atomic layer deposition of vanadium oxide (V_2O_5) was completed in a Beneq TFS-500 ALD reactor. Vanadyl triisopropoxide (VTOP) and water were used as the two precursors during the V_2O_5 baseline recipe at a base pressure of 0.7 mbar and 120° C. First, the VTOP was pulsed for 1 s followed by a 2 s purge time. Water was then pulsed for 2 s followed by a 1 s purge time. The deposition rate of V_2O_5 was 0.3 Å/cycle.

Mesoporous silica was synthesized in the nanostructured alumina membrane using an established recipe.[136] Briefly, the synthesis solutions were prepared by mixing 2.08 g (10 mmol) of tetraethoxysilane (TEOS), 1.8 g (0.1 mol) of water, 3.0 g of hydrochloric acid (0.2 M), and 3.95 g (86mmol) of ethanol. The TEOS-containing solution was brought to 60° C for 1 h for prehydrolysis. The surfactant Brij 56 was measured out to 906 mg (1.33mmol) and was dissolved in 11.85 g of ethanol. After allowing the TEOS solution to cool, both solutions were combined. The alumina templates were dried for 1 h in 110° C in air then placed in ethanol solution for approximately 10 min. The alumina template was then placed in the mixed solution and stirred vigorously for 10 min. After mixing, the template was removed and allowed to dry in air.

The alumina templates with and without deposited materials were structurally characterized using a field emission scanning electron microscope (Hitachi SU-70 SEM). The samples were prepared for SEM by carefully bending the sample and adhering the template on carbon tape to the SEM specimen holder. The mesoporous silica nanostructures were characterized after removal of alumina template. Briefly, the SiO_2 was mechanically polished on the top surface of the membrane. After SiO_2 top layer removal, the SiO_2/alumina template was submerged into 25% wt. phosphoric acid for 18

h. After filtering the samples through centrifuge, the SiO_2 nanostructures were placed on a Cu grid using 6 μL of 1:1 water:ethanol. Imaging of the dispersed SiO_2 nanostructures took place in SEM.

4.3 Results and Discussion

Modification of AAO Pore Walls

Homemade AAO templates were prepared using a well-studied two-step anodization process with modifications to the second anodization step. AAO was prepared in 0.3 M oxalic electrolyte for the growth of nanopores with pore diameter ranging from 30 nm up to 90 nm with an additional pore-widening step. During the second step, the anodization voltage was modified while all other parameters stayed the same as the first anodization process. As seen in Figure 4.2, the voltage was dropped in two-volt increments from the ordering regime of 40 V to a lower voltage of disordering nature. The ordering regime of nanopores in oxalic acid has been well studied. The growth of well-ordered AAO nanopores occurs at 40 V and deviation from this voltage results in an altered pore formation ordering.[71] The lower voltage was typically dropped to 20 V, however, we studied the affect of dropping the voltage to a lower voltage of 14 and 6 V. As the voltage was ramped down to a lower voltage new pores were initiated within the original nanopore. These new channels had a tendency to grow slightly lateral or at an angle within the original pore structure. The original pore walls were basically being 'thinned' out by the application of a lower voltage. Once the voltage reached a set lower voltage, the voltage was then ramped back up to the ordering regime at 40 V at two-volt, 30 s increments, the inverse rate of ramping down. The anodization voltage was held at the ordering regime of 40 V for several minutes.

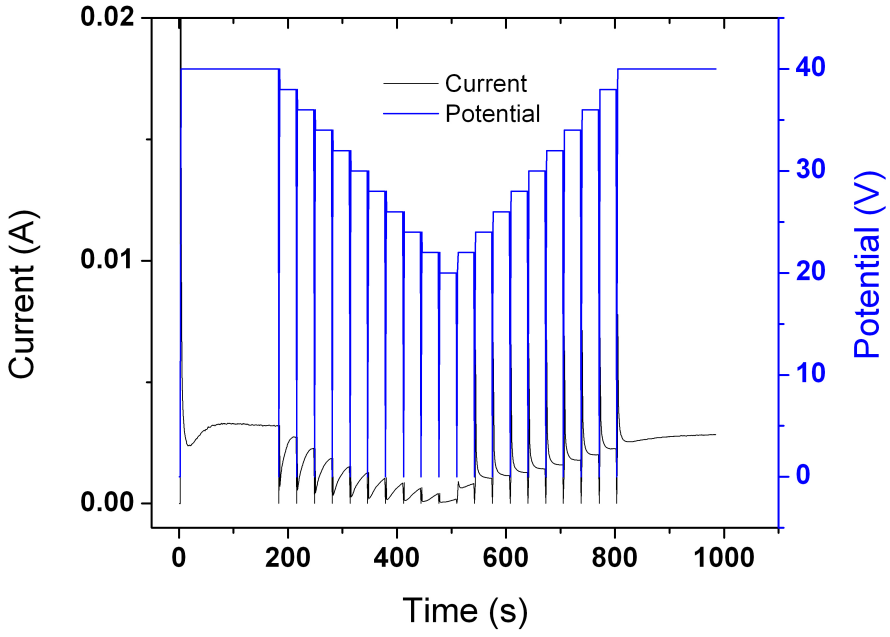

Figure 4.2 Current fluctuations observed during the second anodization ramping step. The ramping occurred at two-volt increments held for 30 seconds.

An important discovery was that once the voltage reached 40 V again, the pore continued to grow in the direction of the original pore. This phenomenon allowed for nearly complete ordering of nanopores before and after the ramping step. The ramping steps were repeated two to three times in some samples, showing the consistent nature of this process. Scheme 4.1 is a representation of the initial ordered pore growth followed by the branching that occurs during the voltage ramping process and finally a pore widening step that opens the pore wall to the neighboring parallel nanopore. A portion of the pore wall remains (dotted line) after the pore-widening step, which allows for enough structural support between the top and bottom sections of the nanopore.

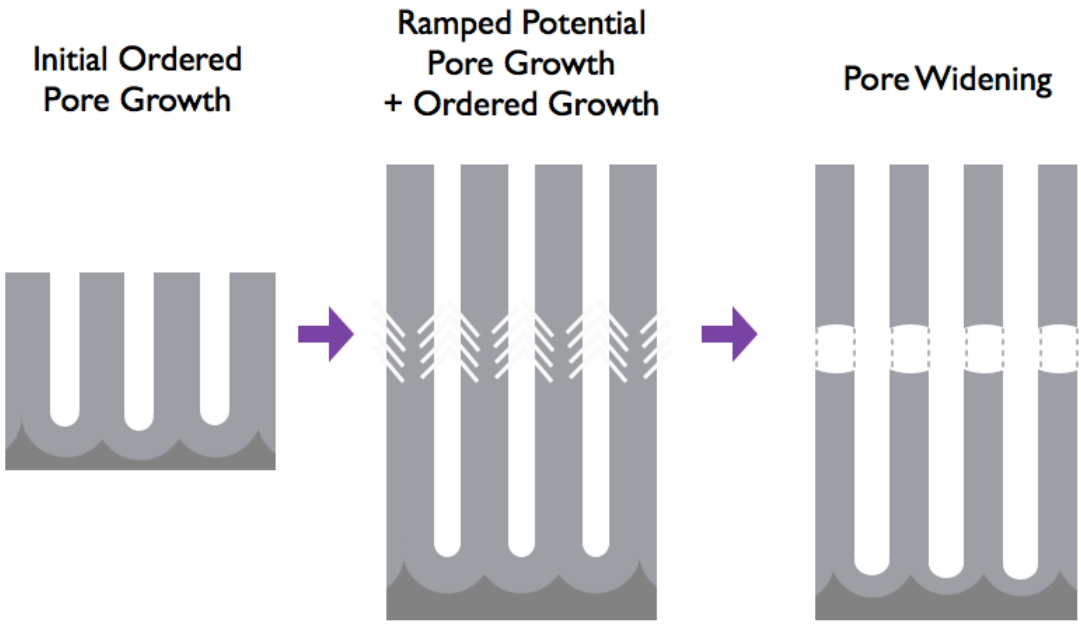

Scheme 4.1 Schematic illustrating regular AAO pore wall formed at a single applied ordering voltage, branched AAO pore wall with step-like branching formed during the voltage ramping, and the pore wall after a pore widening process. The dotted lines in the final image indicate the presence of a portion of the pore wall available for structure support between the top and bottom pore sections.

Figure 4.3 shows an SEM image of an AAO sample that was ramped up and down for two cycles. The disordering or branched area is labeled in the red region where the voltage was dropped from 40 to 20 V. The blue region shows the more smooth nanoporous structure of the 40 V, ordering regime. The figure also shows the voltage steps and current fluctuations that occurred during this process. No pore-widening process occurred in this sample.

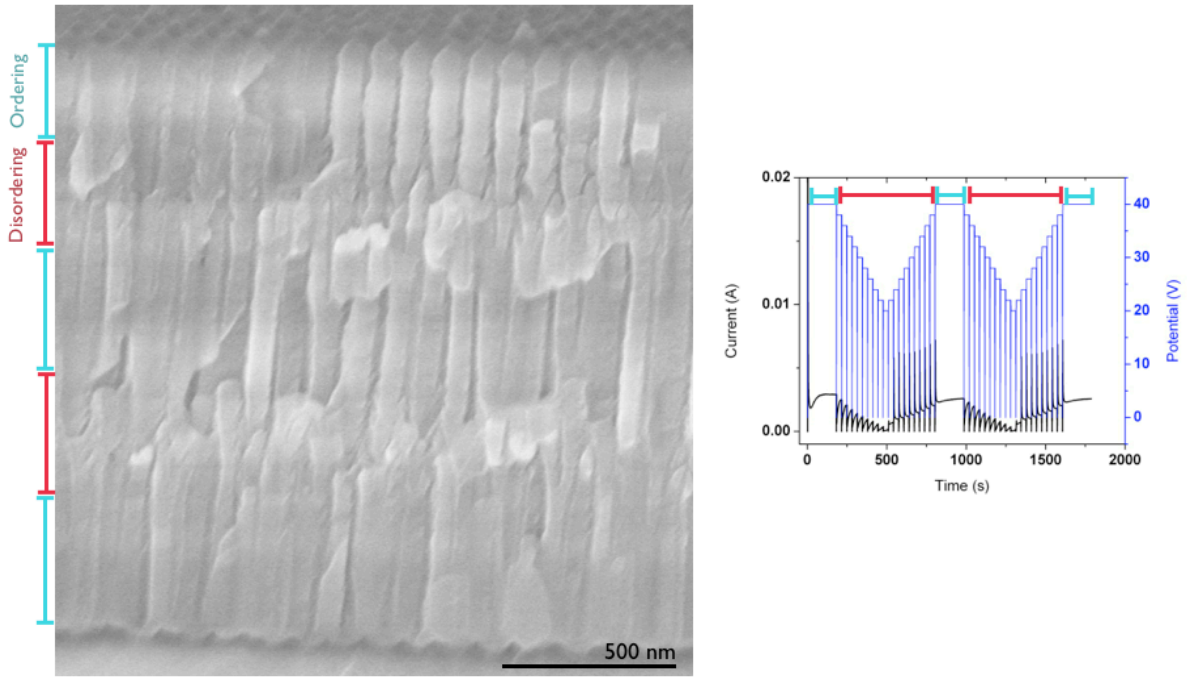

Figure 4.3 SEM image showing the ordering and disordering within AAO nanopores. The ordering region (blue) occurred at 40 V and was maintained for 180 s. The disordering process (red), occurs when the voltage is ramped to a lower voltage out of the ordering regime of AAO and back to the ordering voltage at the same rate. The corresponding current and potential over the anodization time are shown.

Multi-tier Nanostructure

The ability to repeat the ramping down and ramping up of the voltage was demonstrated. Figure 4.4 shows ramping up and down (a) once, (b) twice, and (c) three times with a period of ordering before and after each ramping process. The images displays the clear regions of the cycles. The nanostructures represented in the SEM images in Figure 4.4 were also treated with a pore-widening step as discussed later. The minimum voltage in all three samples was 20 V. The corresponding current for the sample ramped three times is shown in Figure 4.5. The current shows nearly identical

behavior for all three ramping steps. This ideal behavior likely contributes to the repeating behavior for multiple ramping steps and allows for the anodization to continue growing in the original nanopore.

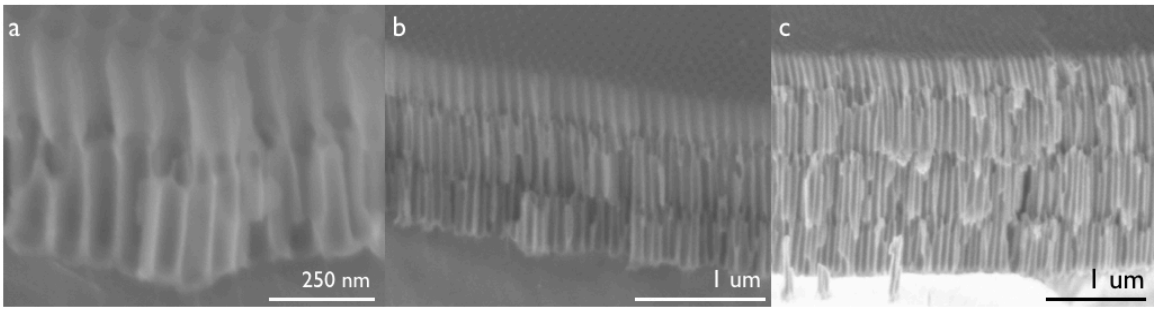

Figure 4.4 SEM images showing the ability to repeat the ramping process of ordered and disorded nature of AAO pore growth. (a) One cycle (b) two cycles, and (c) three cycles of ramping the voltage followed by an identical pore widening process are shown.

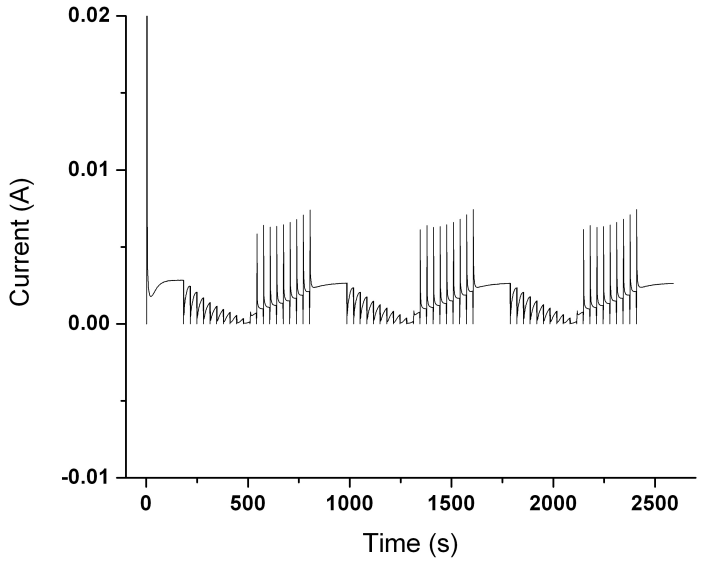

Figure 4.5 Current versus time plot of a sample ramped three times during the second anodization step. The current is nearly identical in all three ramping stages.

Altering Minimum Anodization Voltage

The lower voltage was also altered for different samples to show any variation in the effect of the total ramping voltage window. In Figure 4.6, the images show AAO templates before and after a pore-widening process with varying voltages. For example Figures 4.6 a and d show SEM images of a pore structure that was originally anodized at a voltage of 40 V, creating well-ordered pores. The voltage was then lowered to 6 V through two-volt increments that were each held for 30 s. After 30 s at 6 V, the voltage was increased to 40 V at the same rate. The process was repeated for separate samples with a minimum voltage of 14 and 20 V. Figure 4.6 shows the varying voltage minimums for 6 V, 14 V, and 20 V before (Figures 4.7 a, b, c) and after (Figures 4.6 d, e, f) pore-widening.

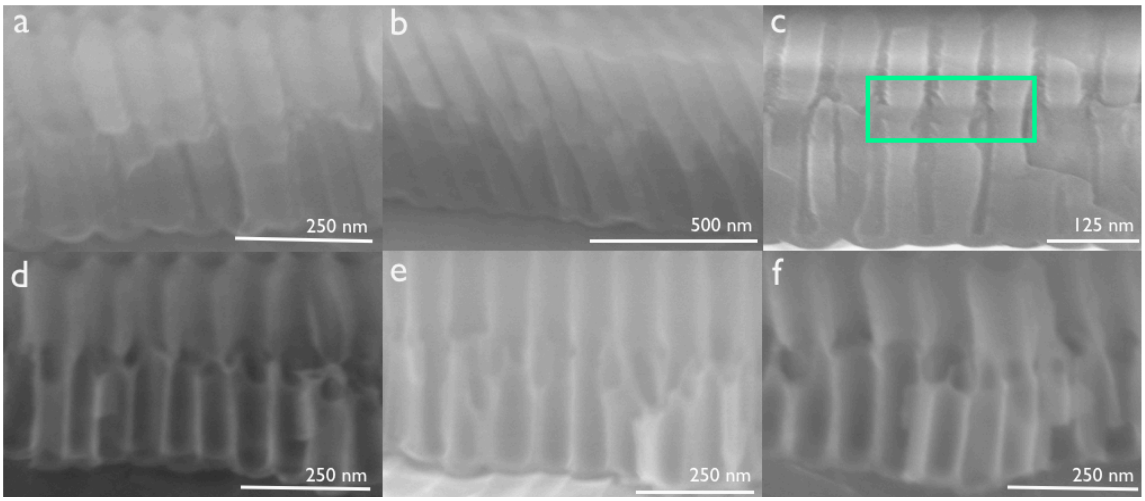

Figure 4.6 SEM images illustrating the result of altering the minimum voltage for the second anodization step. (a), (b) and (c) The AAO porous structure at a minimum anodization voltage of 6 V, 14 V, and 20 V without pore-widening, respectively. (d), (e), and (f) The result of the pore-widening step after the second anodization process at 6 V,

14 V and 20 V, respectively. The green box in (c) highlights the branched region during the ramping process.

The currents for the varying voltage minima are compared in Figure 4.7. The current reveals interesting information about the anodization conditions for each of the three samples. It appears that during the ramping down process, the 6 V and 14 V currents are similar. However, during the ramping up stage, the current for the 14 V sample is more similar to that of the 20 V sample. This effect is perhaps due to the 'extreme' low current of the 6 V. As one can see in Figure 4.7, the 6 V current for the lowest voltages is very small.

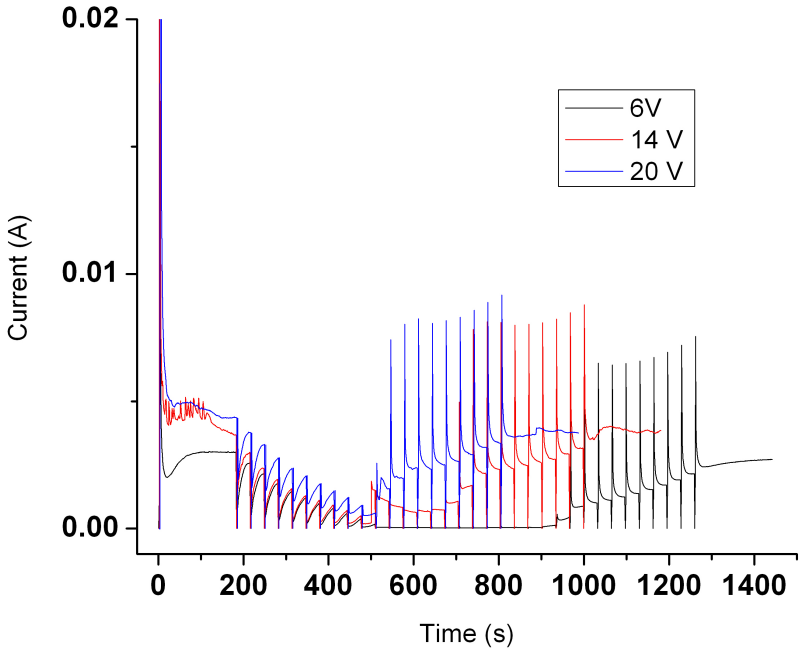

Figure 4.7 Current versus time plot of samples with varying minimum ramping voltages (6, 14, 20 V) with the same ramping steps (two-volt, 30 s increments).

Chemical Etch Process to Create Nanoporous Interconneting Network

In order to create interconnecting porous nanostructures, the AAO template underwent a pore-widening or chemical wet etch process after the voltage ramping step. The pore widening solution consisted of a 5% wt. H_3PO_4 in water solution at a controlled temperature of 38° C. The solution was gently stirred throughout the process. The pore-widening step etches the walls of the alumina structure as well as slightly etching the porous bottom barrier layer. This process was optimized for the pore widening time in order to make a hole-like structure at the disordering or branching section of the nanopores. Figure 4.8 shows the result of pore-widening the AAO template over a period of 0 to 20 minutes. It is likely that prior to a 20 min pore-widening process, the AAO template is completely delaminated from the bottom Al layer. Through SEM images it was determined that 10-12 minutes was the ideal pore widening time for nearly complete removal of the nanopore wall at designated areas.

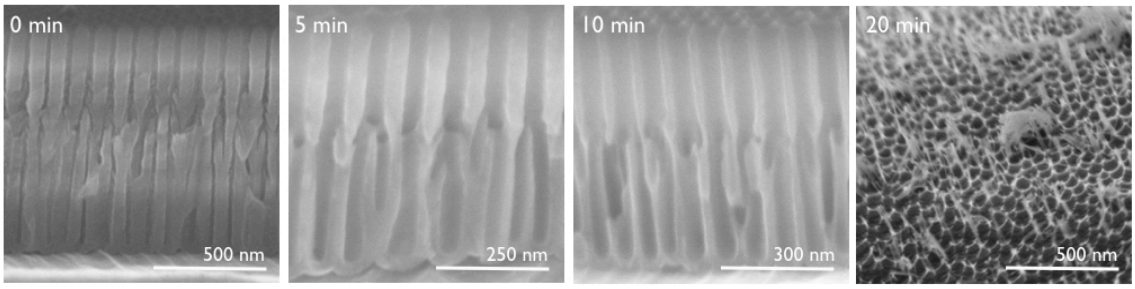

Figure 4.8 SEM images showing the result of a pore-widening step in phosphoric acid over a period of 20 minutes. The experiments led to the conclusion that a pore-widening step of 10-12 minutes was ideal for opening neighboring nanopores.

Barrier Layer Thinning and Removal

The next technique in the process is the modification of the barrier layer at the pore bottom. The key difference between this modification and the previous one lies in the ramping process of the anodization potential. In the first technique, the potential was ramped in a step-wise manner, creating new pore channels along the pore walls. The potential was held at a reduced voltage for a greater length of time. In the barrier-layer modification process, the potential is continuously ramped followed by a period of constant 'disordering' applied potential. The barrier layer thickness is reduced by the gradual decrease in potential followed by a chemical etching process that completely removes the bottom barrier layer, thus providing access to the bottom Al substrate (Scheme 4.2). This process is shown in Scheme 4.2 starting with a typical barrier layer thickness at a constant 40 V, followed by a reduction in the barrier layer thickness due to the voltage ramping and finally a pore-widening process to remove the remaining barrier layer.

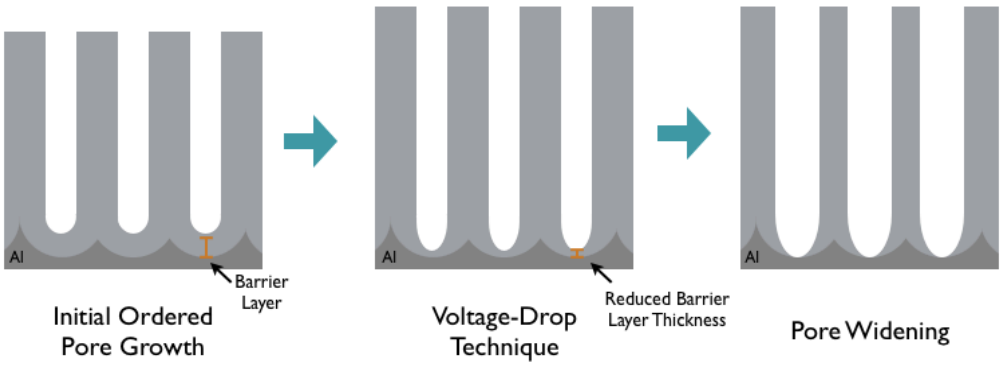

Scheme 4.2 Process for the removal of the barrier layer of the AAO pore structure using a modified anodization step of ramping the potential followed by a pore-widening or chemical etching process.

The voltage drop technique is shown in Figure 4.9. The initial pore formation occurs at the 'ordering' regime for oxalic acid at 40 V. After a set time, the potential is reduced at a set rate using the appropriate parameters in the LabView VI. It was determined based on imaging results (as discussed below) that the ideal ramp rate was 0.09 V s^{-1}. After the ramping step, the potential was held at a constant 15 V for 900 s.

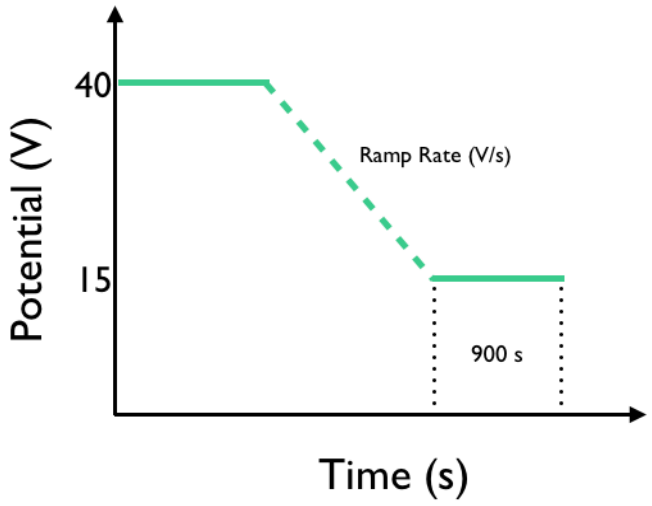

Figure 4.9 Plot depicting the voltage drop technique. There is a period of pore 'ordering' growth at 40 V followed by a potential decrease at a set rate and finally a short period of constant lowered potential (15 V).

Figure 4.10 shows SEM images of samples created using the three different ramp rates: (a) 0.01, (b) 0.03 and (c) 0.09 V s^{-1}. Due to the total increased time that occurred during ramping at the slower ramp rates, there was significantly more branching that occurred on the pore bottom. This situation is not ideal for complete removal of the barrier layer. Once the ramp rate was increased to 0.09 V s^{-1}, we observed greater thinning of the bottom barrier layer and less branching. The minimum potential of 15 V was held

constant at the end of the second anodization for 900 s in all samples. Figure 4.11 shows the current change observed during the ramping process at 0.01, 0.03 and 0.09 V s^{-1}. For the sample ramped at of 0.09 V s^{-1}, one can see that prior to reaching 15 V, the current has reached a steady-state value.

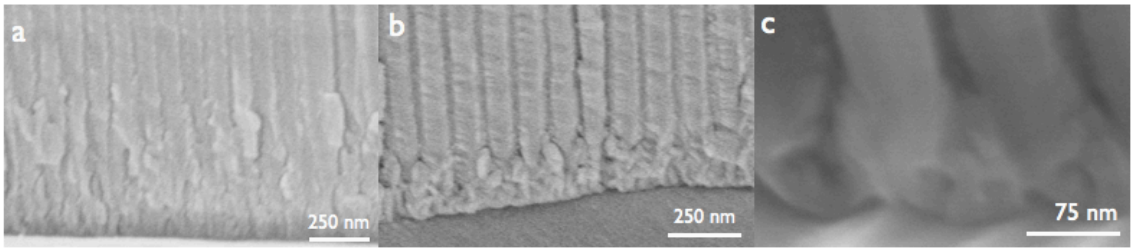

Figure 4.10 SEM images of samples created at varying ramp rates for the decrease in anodization potential to a minimum of 15 V. (a) 0.01, (b) 0.03 and (c) 0.09 V s^{-1} ramp rates.

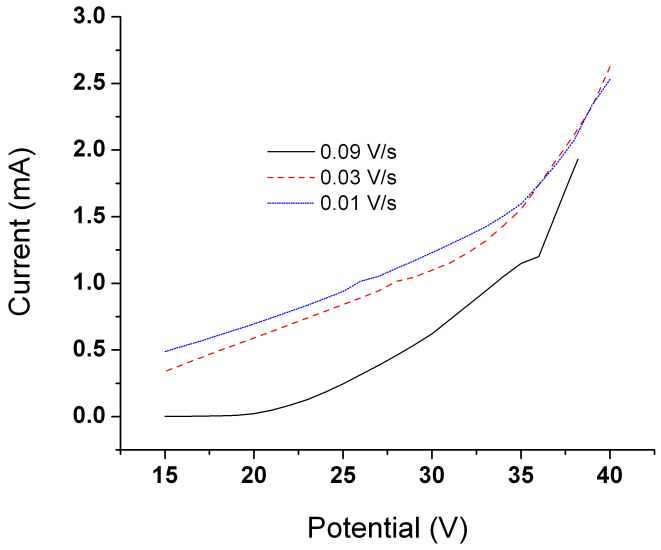

Figure 4.11 Current versus potential plot at varying ramp rates. 0.01 V s^{-1} is represented by the blue solid line, 0.03 V s^{-1} is represented as red dotted line and 0.09 V s^{-1} is shown as black solid line.

Following the voltage-drop technique a chemical etching process takes place and the barrier layer is completely removed. The chemical etching process was observed over a range of times to allow for complete removal of the barrier layer without completely delaminating the AAO pore structure from the Al substrate. Figure 4.12 shows the AAO sample (a) with no chemical etching, (b) after 11.5 minutes of 5% wt. phosphoric acid etching and (c) after 15 minutes with 5% wt H_3PO_4 etching at 38° C. The chemical etching or pore-widening process not only removes the thinned barrier layer, but also etches away the pore walls since they are of similar chemical nature.

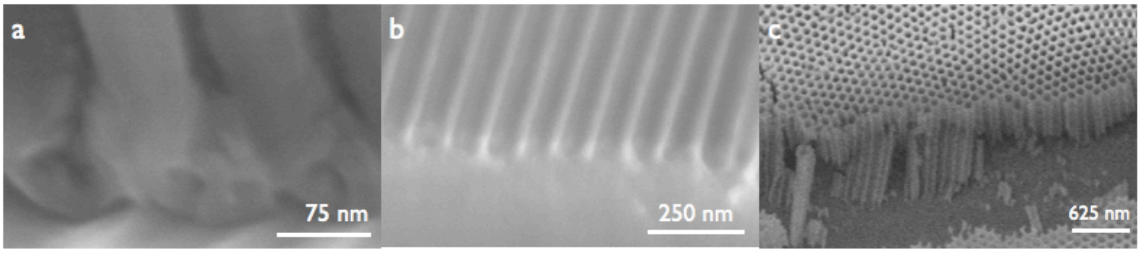

Figure 4.12 SEM images of (a) no pore widening (b) 11.5 min pore widening and (c) 15 pore-widening for 0.09 V s^{-1} samples in 5% wt. H_3PO_4.

Combining AAO Modification Techniques for 3D Nanostructured Design

The barrier layer removal technique is demonstrated here for potential use in the 3D nanostructure template design. The first AAO modification process would allow for an interconnecting branched network to form between neighboring pores. The second modification process (barrier layer thinning) would be applied to the end stages of pore formation, thus reducing the barrier layer thickness. A final pore widening or chemical etch step would satisfy both modifications by opening the branched pore walls and the bottom barrier layer. It was found that a pore widening time of approximately 10-12

minutes in 5% wt. H_3PO_4 allowed for both the etching of pore walls and the removal of the barrier layer. Thus, both processes can potentially occur simultaneously. The resulting 3D nanostructure would allow for deposited materials between walls as well as connecting them to the bottom Al substrate. The Al substrate could also be used as a working electrode for further electrochemical deposition techniques.

Deposition within the 3D Nanoporous Network

ALD of vanadium oxide was used to create a 3D network of nanomaterial. After fabrication of the alumina template and a pore-widening process to open the nanopores as described in the first AAO modification process, V_2O_5 was deposited into the structure using a commercial ALD reactor. The baseline V_2O_5 recipe was used with VTOP and water precursors. 30 nm of V_2O_5 was deposited at 120° C. After deposition within the nanopores, the nanostructures were structurally characterized using SEM imaging. The images shown in figure 4.13 reveal the V_2O_5 films within the interconnected network. It is clear at the majority of opened areas within the pore (at the disordering/branching sites) that the V_2O_5 from separate parallel pores is able to connect to the neighboring pore V_2O_5. This result is visible in both the single branched AAO and doubly branched AAO nanostructure. It is interesting to note that the V_2O_5 was successful at connecting nanopores even within the doubly branched structure in a similar fashion as the single branched structure. This process shows great promise for utilization of ALD within ordered nanoporous structures. The V_2O_5 could not be further modified due to its solubility in aqueous solution. Further ALD studies are underway to examine the ability of the 3D V_2O_5 nanostructure to stand alone after removal of the AAO template.

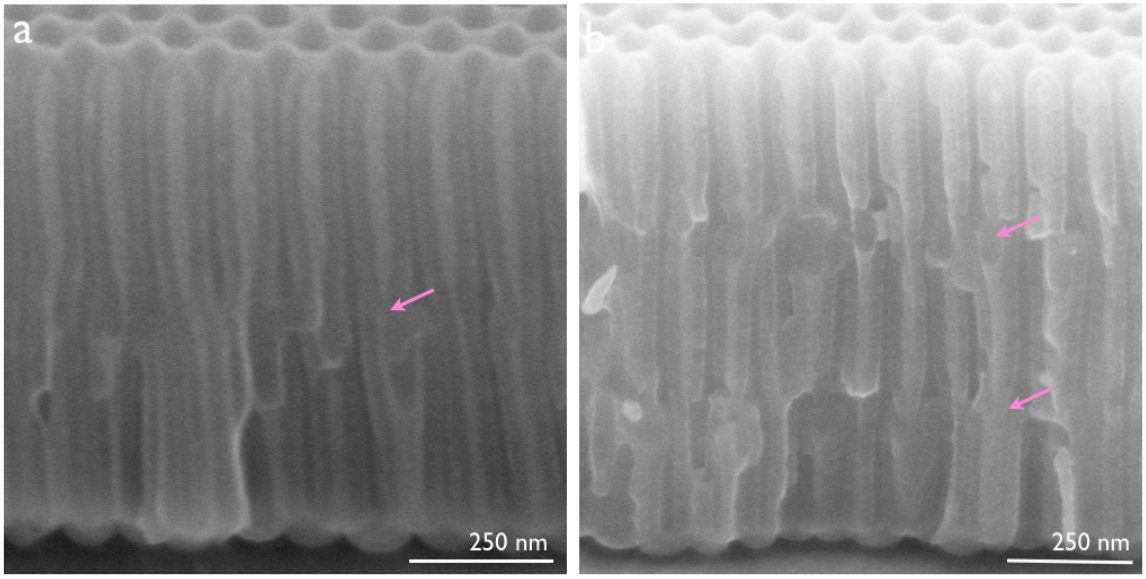

Figure 4.13 (a) SEM image of a single branched AAO structure with 30 nm of ALD V_2O_5 deposited within the pores. The darker color is the V_2O_5 while the lighter color is the AAO template. At the center of the image, the lighter AAO is removed or nearly removed, connecting the V_2O_5 between neighboring pores. (b) SEM image of a doubly branched nanostructure revealing the ability of ALD to deposit V_2O_5 deep within the nanopores and to connect the neighboring pores even in the second branched structure closer to the pore bottom.

To demonstrate the capability of the 3D AAO nanostructure to act as a template for stand-alone architectures, a chemical synthesis method to fill the nanoporous network with mesoporous silica was used. Once the template was prepared with interconnecting pores, the template was heated in the oven for at least one hour at 110° C. The template was then submerged into ethanol for at least ten minutes. These two steps were completed in order to reduce the surface tension of the alumina template and allow for facile synthesis of silica within the porous structure. A solution of TEOS, ethanol, HCl,

and water was prepared as described previously. This solution was heated at 60° C for 1 h for prehydrolysis. The surfactant solution was prepared using Brij 56 and ethanol. Once the TEOS-based solution was cooled to room temperature, the TEOS and Brij solutions were mixed well. The alumina template was then immersed in the mixed solution for ten minutes and stirred vigorously. The silica treated template was allowed to dry in air. The surface silica was removed using a mechanical polishing process. The template was then immersed into 25 % wt. phosphoric acid overnight. After filtering the nanostructure from the acid solution ~ 6 μL was placed onto a Cu grid using a 1:1 ethanol:water solution. The Cu grid was observed with SEM imaging after the sample was dry.

SEM imaging revealed a nanoporous network of silica material as shown in Figure 4.14. The nanopores are of expected dimensions based on the alumina template. Although Figure 4.14 does not offer clear evidence of interconnecting pores, we believe that with further investigation through imaging and silica synthesis modification we will achieve a continuous connection between parallel pores.

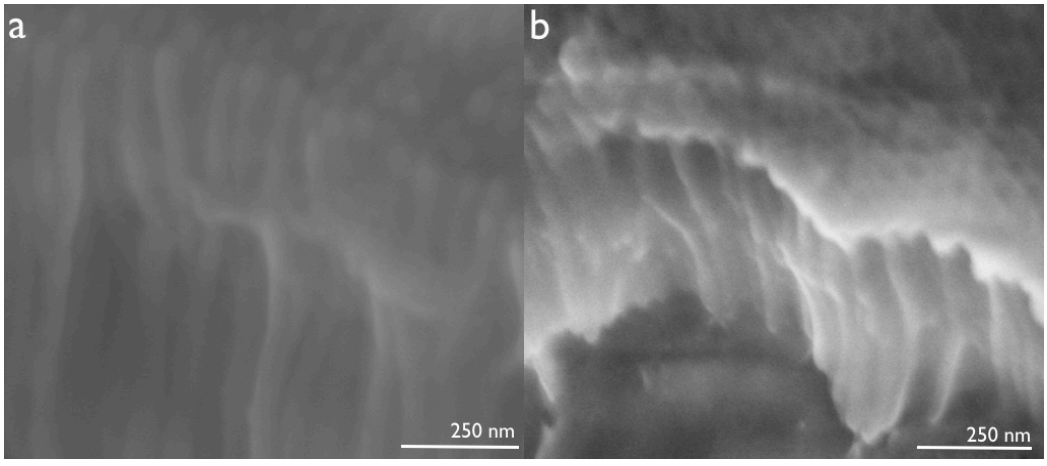

Figure 4.14 (a,b) SEM images showing stand-alone mesoporous silica nanostructure after removal of the AAO template.

ALD and chemical synthesis have provided initial confirmation that the nanoporous structure is indeed connected between parallel nanopores. With continued efforts in other self-limiting deposition modifications, this 3D interconnecting nanostructure may lead to an array of stand-alone 3D nanoporous networks. For example, ALD of titanium nitride (TiN) will provide an excellent film for deposition within the alumina template. Utilizing TiN will allow for electrical characterizations as an energy storage system due to its superior electrical conductivity and chemical resistance to AAO removal process. After removal of the AAO template, the TiN could be combined with electrochemically deposited materials such as MnO_2 for preparation as a supercapacitor electrode material. An additional proposed study includes the nature of the 3D channeling. For example, this 3D nanoporous network could be used in two designs. First, an ALD material could be deposited along the porous walls allowing for an open porous structure to remain for further modification. Secondly, ALD or other chemical synthesized material can be used for the complete filling of the nanopores. Figure 4.15 shows these two processes schematically. The figure also illustrates the use of the bottom Al substrate from the removal of the barrier layer. The Al substrate provides an ideal bottom layer for further use as an electrode. Interesting results are likely to come from both designs, especially from electrical characterization of ion movement.

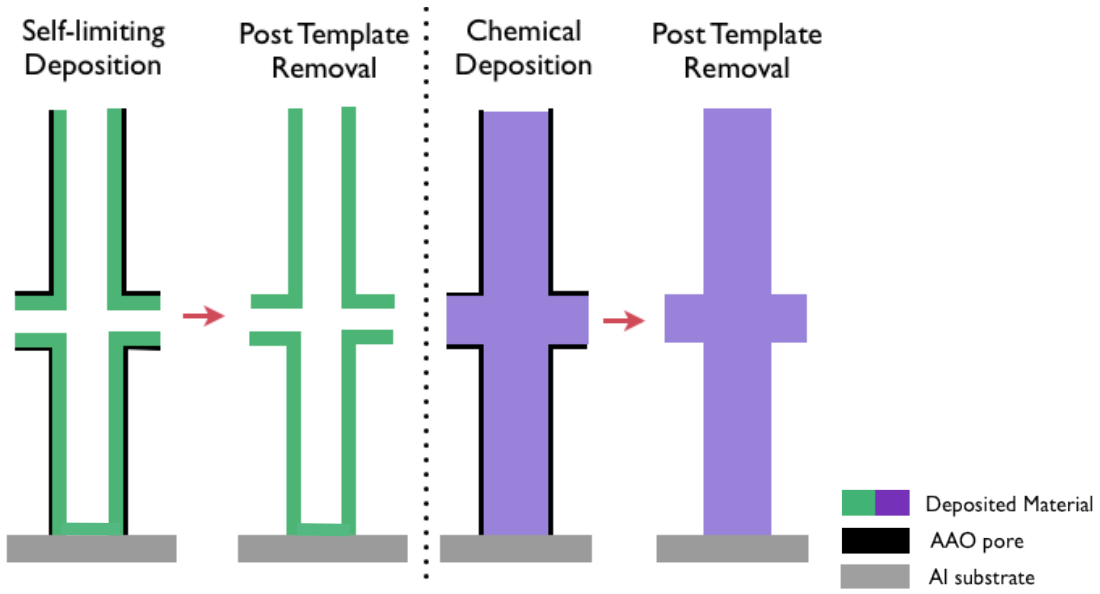

Figure 4.15 Two proposed schematics for the fabrication of 3D porous networks utilizing ALD, ECD or chemical synthesis processes. The deposited material is introduced to the modified AAO template followed by the template removal for stand-alone 3D nanostructures

4.4 Conclusion

In summary, we have described the foundation and initial structural characterizations of a 3D nanoporous network based on the modification of an AAO template. This highly controlled interconnecting porous structure is a vital template synthesis method for future heterogeneous nanostructured materials for a variety of applications including electrochemical energy storage. By simply ramping the anodization voltage at a controlled rate, the AAO walls were thinned. This process allowed for further etching using a chemical pore widening process to open up the neighboring walls of parallel pores. Due to the high level of control of branching, multiple connections can form throughout a single nanopore. Using a self-limiting

deposition technique such as ALD, thin conformal films were deposited within the intricate design. The use of the AAO template for fabrication of stand-alone materials by removal of the alumina template was also demonstrated using the synthesis of SiO_2.

A second AAO modification process was demonstrated and showed the ability to remove the barrier layer, thus creating a pathway from the nanopore to the bottom Al substrate. This process was completed using a slightly different voltage ramping process and similar chemical etching step. These two modifications combined would yield a 3D interconnecting network with access to a conductive Al substrate. The full potential of this highly controlled 3D nanoporous template has not yet been realized, but this work has laid a foundation for further innovative fabrication. Certain challenges remain with this 3D design as well as future 3D nanostructures including the characterization and understanding of physical, chemical and electrochemical interactions.

Chapter 5: Summary and Outlook

5.1 Summary

The overall goal of this research was to design, fabricate, and characterize electrochemical energy storage technology based on template prepared nanostructures. Using well-ordered AAO template with highly controllable dimensions, heterogeneous nanostructures were successfully fabricated by combining favorable electrical energy storage materials.

This dissertation conveys three main results:

(1) the combination of self-limiting atomic layer deposition with electrochemical deposition to construct novel nanostructures,

(2) the enhanced capacitance of a supercapacitor electrode based on an AAO-based heterogeneous nanostructure design and,

(3) the modification of AAO for the development of novel, well-ordered 3D interconnecting nanostructures.

The first result provided a unique opportunity to demonstrate the use of suitable deposition techniques within high-aspect-ratio nanostructures. The combination of ALD and ECD within a nanostructured template has not been well studied. In this dissertation, the approach to the fabrication of heterogeneous nanostructures resulted in improved specific capacitance and provided a foundation for future innovative nanostructured designs. The combined nanostructure was characterized in detail using analytical tools. These studied provided insight into the chemical, structural, and electrical features of these structures.

Another result of this dissertation was the development of heterogeneous nanostructures for improved capacitance for use in electrochemical energy storage systems. Utilizing an AAO template and favorable energy storage materials (TiN, MnO_2), nanotubular arrays were constructed for use as supercapacitor electrodes and resulted in significant increases in specific capacitance compared to previous work based on heterogeneous nanostructure systems. The large increase in surface area gained from using both the inner and outer surface of the TiN nanotube provided a considerable enhancement in charge storage.

Finally, a novel 3D nanostructured design based on the modification of regular AAO templates was demonstrated. By ramping the anodization potential during pore formation, a unique branched design that thinned the pore walls was achieved. After a pore-widening step, the neighboring nanopores were connected and an interconnecting nanoporous network was provided. The ability to control the branching of the AAO nanopores presents a novel route for the development of well-ordered 3D nanostructures. A second AAO modification process was demonstrated that provide access to the bottom Al substrate by thinning the AAO barrier layer. This access to the Al substrate allows for interesting and perhaps more straightforward 3D designs. Successful deposition of materials within the 3D nanostructure was also demonstrated and laid the foundation for future characterization and understanding of 3D nanostructures especially those intended for use in electrochemical energy storage.

5.2 Outlook

This work has brought to light several key ideas for the design and fabrication of electrochemical energy storage technologies. Innovative techniques such as combining

ALD and ECD can be utilized in a variety of nanostructured designs for improved electrical properties. The continued focus on combining favorable electrode materials will likely generate improved synergistic effects and provide new opportunities for further understanding of the fundamental chemical and electrical interactions. The study of multidimensional nanostructures, especially 3D nanostructures, is still in its infancy, yet multidimensional nanostructures could potentially generate drastic improvements in energy and power for electrical energy storage systems. By preparing well-ordered nanostructures we may investigate, in a systematic way, the electrical and ionic interactions at the electrode surface. A deeper understanding of these interactions may very well lead to improved energy and power density of electrical energy storage systems.

Appendix:

A.1 ALD TiN Baseline Recipe

*Recipe TiN_Baseline_175C_1000Cy

*Recipe TiN 60nm@175C, 300 cycles

*Precursors TDMAT and Ammonia

*pban@umd.edu , 2008 october 30

*Based on flow chart N500112

*TDMAT at Hot Source2

*Ammonia at gas source 1

*Source needle valves (NV-PL1 open 1/2 turn, NV-PL4 open 1 turn, NV-PG1 open 1 turn)

*Inert gas drain valves (NV-IA open 1.5 turn, NV-IB open 1/2 turn

*Chiller temperature 20C

*TDMAT temperature 30C

*growth rate 1.3A/cy (measured on SOPRA 11/25/08)

*Program start

SPROG

*Open the N2 main valve

OPEN DV-N01

*Set flows

FLOW MFC-AS=100

FLOW MFC-BS=100

FLOW MFC-VS=100

```
*Close pulse valves
CLOSE DV-PL1,DV-BL1,DV-PL4,DV-BL4
CLOSE DV-PG1,DV-PG2,DV-PA,DV-PB
*Close hot source valves
CLOSE DV-BHA1,DV-BHA2,DV-PH1,DV-PH2
CLOSE DV-BH1,DV-BH2
*Check the vacuum level
        WUNTIL PIA-P1<10 2s
*Set temperatures
        TEMP TIAC-R1S=175
 *wait until temperature is ok
        WUNTIL TIAC-R1>=TIAC-R1S 5h
*Are temperatures ok to start the process ?
WRITE M5
WUSER YES
*Purge hot source 2 source tube before run
Pulse DV-BHA2 5s
*Pulsing TDMAT and Ammonia 1000 cycles,
REPEAT 1000
            PULSE DV-BHA2,DV-BH2 500ms
            PULSE DV-PH2 1s500ms
            PULSE DV-BHA2,DV-BH2,DV-PH2 500ms
            PURGE 500ms
```

```
        OPEN DV-PA
        WTIME 250ms
        PULSE DV-PG1 500ms
        WTIME 300ms
        CLOSE DV-PA
        PURGE 2s
REND
*Empty residual precursor from hot source 2 source tube after run
PULSE DV-BHA2 5s
PULSE DV-PA 5s
*Set temperatures
*       TEMP TIAC-R1S=20
*Close pulse valves
CLOSE DV-PL1,DV-BL1,DV-PL4,DV-BL4
CLOSE DV-PG1,DV-PG2,DV-PA,DV-PB
*Close hot source valves
CLOSE DV-BHA1,DV-BHA2,DV-PH1,DV-PH2
CLOSE DV-BH1,DV-BH2
*Use gas ballast 1 min
PULSE DV-NP1 1min
*end program
EPROG
```

A.2 X-ray Diffraction

X-ray diffraction is an analytical technique used to reveal information about a material's crystal structure, chemical composition and physical properties. Below is a sample XRD taken of an electrochemically deposited MnO_2 film and ZnO within an alumina template. The results indicate the presence of multiple phases or structures of manganese oxide present.

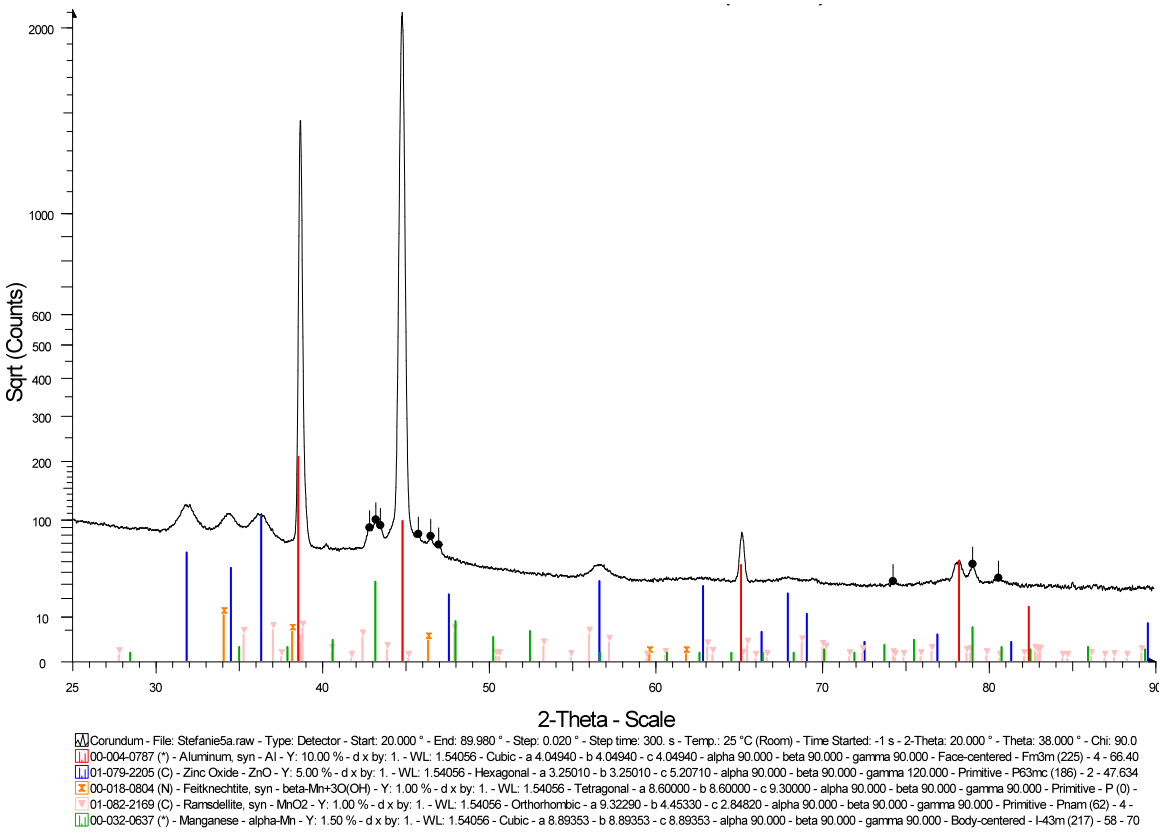

Figure A.1 XRD analysis of MnO_2/ZnO nanostructure within an alumina template.

A.3 Raman Spectroscopy

Raman spectroscopy is a chemical analysis technique that provides information used to study the vibrational, rotational, and other low-frequency modes in a sample. Since the vibrational information is specific to chemical bonds and the symmetry of

molecules, it is commonly used in the field of chemistry. Raman spectroscopy relies on the inelastic scattering, or Raman scattering of monochromatic light, generally from a laser in the visible, near infrared, or near ultraviolet range. The laser interacts with molecular vibrations, phonons, or other excitations in the sample, which result in the energy of the laser photons being shifted up or down. This shift in energy gives rise to information about vibrational modes in the system.

Raman spectroscopy was used to further identify and characterize the MnO_2 material that was electrochemically deposited. Figure A.2 shows the Raman shift of MnO_2 at 631 cm^{-1} using a 532 nm green line laser from a Horiba Yvon LabRam ARAMIS Raman Microscope.

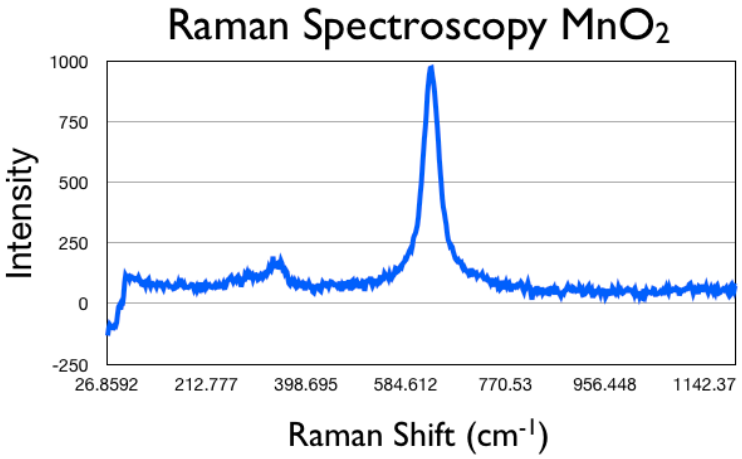

Figure A.2 Raman shift of MnO_2 sample using a 514 nm laser.

A.4 X-ray Photoelectron Spectroscopy (XPS)

X-ray photoelectron spectroscopy (XPS) is a surface chemical analysis technique that can be used to analyze the top 1-10 nm of a material. This quantitative analytical technique measures information such as the elemental composition, empirical formula,

chemical state and electronic state of elements on a sample material. The spectrum obtained in XPS is a plot of the number of electrons detected versus binding energy of the electrons. These spectra depict the kinetic energy and number of electrons that escape from a material when it is irradiated with an x-ray.

The XPS data provided here is of TiN/Al-doped ZnO films on glass. The data reveals that there is a tendency of TiN to oxidize near the surface of the film. This is shown as a slight shoulder within the Ti peak of both Figures A.3 i (20 degree) and A.3 ii (90 degree). As previously mentioned, this oxidation may hinder the capacitance capabilities of TiN for use as an electrode material.

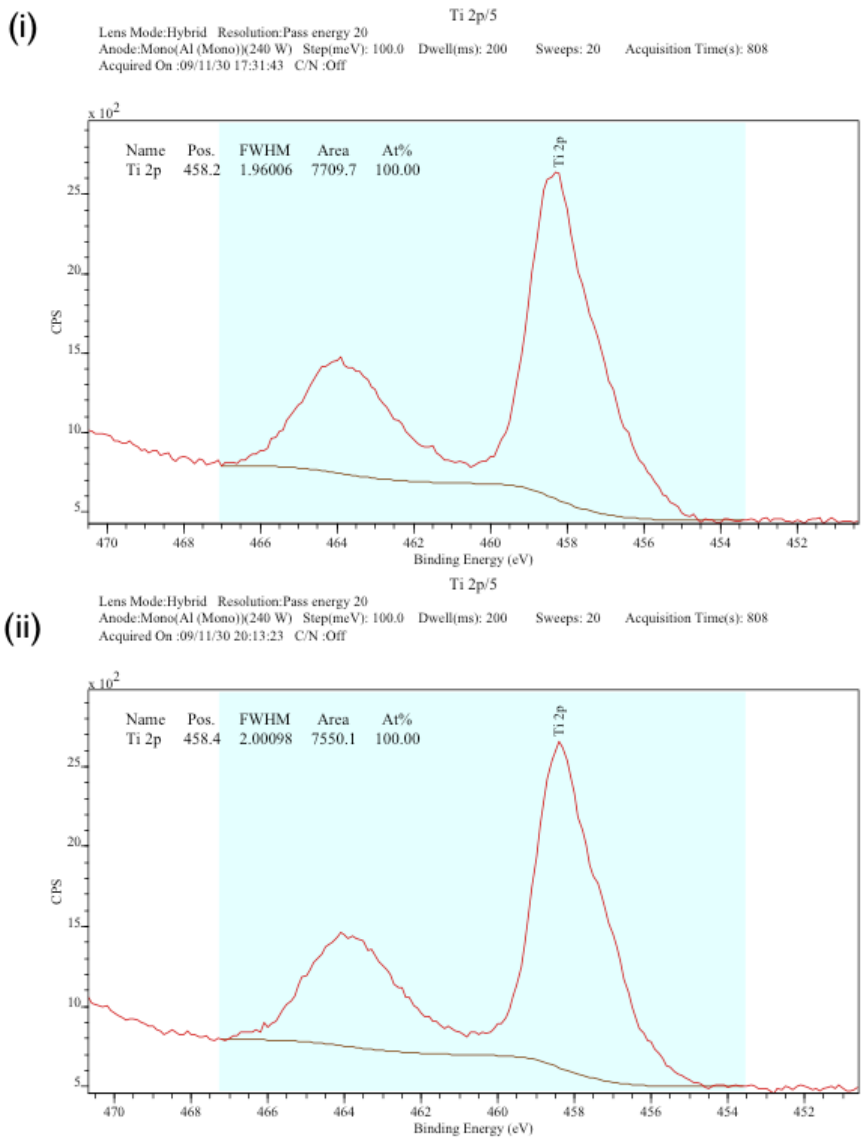

Figure A.3 (i,ii) XPS data obtain from TiN/Al-doped ZnO on glass substrate showing a slight shoulder on the Ti peak possibly indicating the presence of oxygen. (a) Results from 20 degree analysis and (b) 90 degree analysis

A.5 AAO Sample Holder:

The second anodization process for preparation of 3D nanostructures was completed in a homemade sample holder "Herbie." Herbie is the second generation of

sample holders for anodization of aluminum in Dr. Lee's lab. Al foil that had previously gone through pre-treatment, first anodization and etching was cut into 16x16 mm pieces. An area of 1.27 cm^2 was exposed to the anodization electrolyte. The Al was connected to the anode of the power source through Cu tape (3M). The counter electrode was a stainless steel mesh connected to the cathode of the power source.

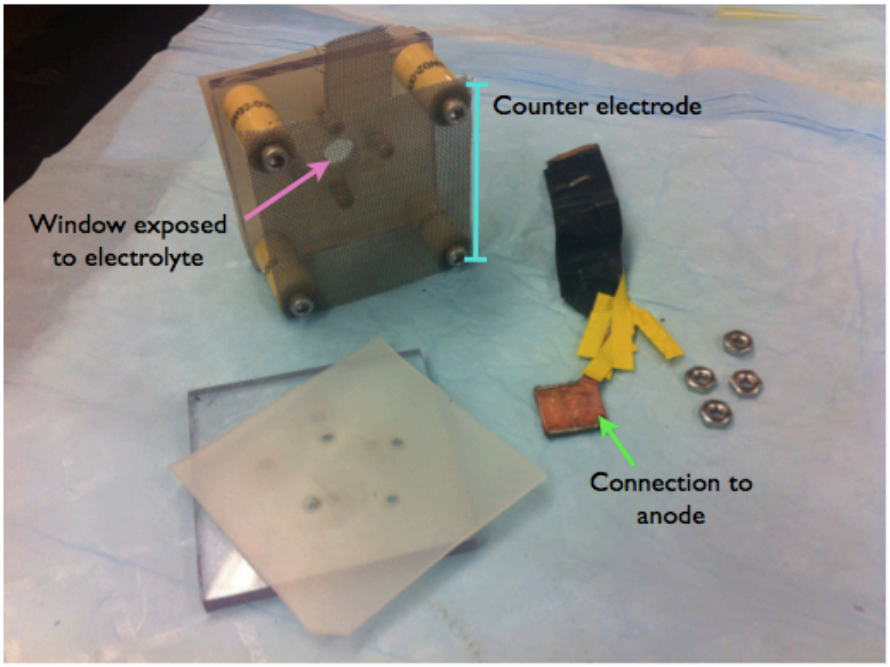

Figure A.4 Sample holder for one-sided confined anodization of aluminum

A.6 Controlling the Voltage During Anodization Step

National Instrument's (NI) Labview software, integrated with a Keithley 2400 source meter, was utilized to control the voltage setting during second anodization of the 3D alumina template. The LabView VI was originally developed by Dr. Parag Banerjee. Recipes were built to ramp the voltage up and down during the anodization process. The VI also connects to a circulator for precise control over temperature. Real-time graphs

display several parameters (temperature, time, current, voltage, and charge) of the system. Screen shots of the front panel and block diagram are pictured in Figure A.5.

(i)

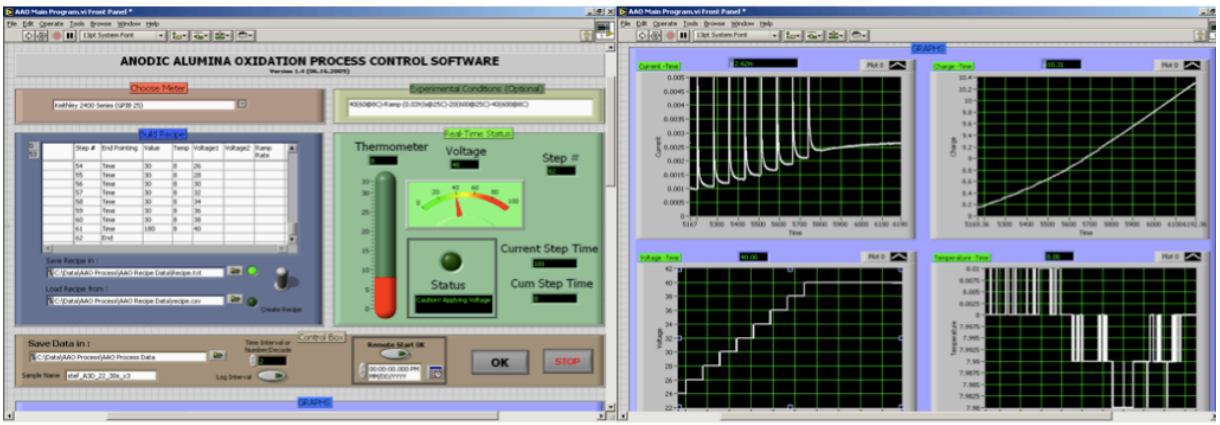

(ii)

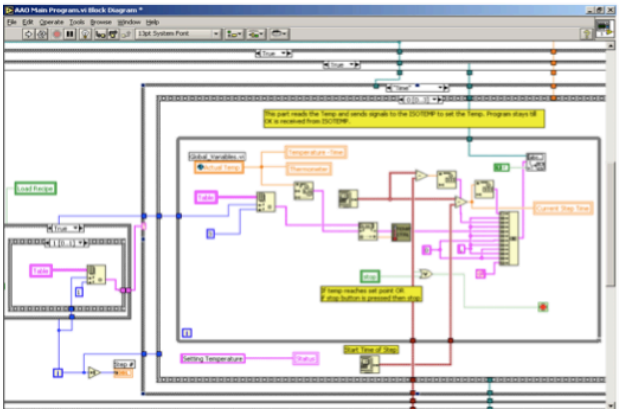

Figure A.5 (i, ii) Screen image of NI LabView VI (i) front panel and (ii) block diagram

Publications

Portions of Chapter 2 have been published in
Phys. Chem. Chem. Phys., **2011**, *13*, 20714-20723

Chapter 3 in this dissertation has been published in
Phys. Chem. Chem. Phys., **2011**, *13*, 15221-15226

References

(1) Long, J.; Rolison, D. *Electrochemical Society Interface* **2008**.
(2) Hall, P.; Mirzaeian, M.; Fletcher, S.; Sillars, F. *Energy & Environmental ...* **2010**.
(3) Burke, A. *Journal of Power Sources* **2000**, *91*, 37–50.
(4) Rolison, D. R.; Long, J. W.; Lytle, J. C.; Fischer, A. E.; Rhodes, C. P.; McEvoy, T. M.; Bourg, M. E.; Lubers, A. M. *Chem Soc Rev* **2008**, *38*, 226–252.
(5) Bruce, P. G.; Scrosati, B.; Tarascon, J.-M. *Angew Chem Int Ed Engl* **2008**, *47*, 2930–2946.
(6) Okubo, M.; Hosono, E.; Kim, J.; Enomoto, M.; Kojima, N.; Kudo, T.; Zhou, H.; Honma, I. *J Am Chem Soc* **2007**, *129*, 7444–7452.
(7) Aricò, A.; Bruce, P.; Scrosati, B.; Tarascon, J. *Nature Materials* **2005**.
(8) Kötz, R. *Electrochimica Acta* **2000**.
(9) Simon, P. *Nature Materials* **2008**.
(10) Hamilton, T. Next Stop: Ultracapacitor (accessed Mar. 23, 2012).
(11) Nelson, P. *Journal of The Electrochemical Society* **2003**.
(12) Shukla, A.; Sampath, S. *Current science* **2000**.
(13) Conway, B.; Birss, V. *Journal of Power Sources* **1997**.
(14) Conway, B. E.; Pell, W. G. *Journal of Solid State Electrochemistry* **2003**, *7*, 637–644.
(15) Frackowiak, E. *Carbon* **2001**.
(16) Futaba, D.; Hata, K.; Yamada, T.; Hiraoka, T. *Nature Materials* **2006**.
(17) Pandolfo, A. G.; Hollenkamp, A. F. *Journal of Power Sources* **2006**, *157*, 11–27.
(18) Gamby, J.; Taberna, P.; Simon, P. *Journal of power ...* **2001**.
(19) Lota, G.; Centeno, T.; Frackowiak, E. *Electrochimica Acta* **2008**.
(20) Wang, J.; Zhang, S.; Guo, Y.; Shen, J. ... *Electrochemical Society* **2001**.
(21) Wang, D.-W.; Li, F.; Liu, M.; Lu, G. Q.; Cheng, H.-M. *Angewandte Chemie* **2008**, *120*, 379–382.
(22) Halper, M.; Ellenbogen, J. *Report No MP 05W0000272* **2006**.
(23) Prasad, K. *Applied Physics Letters* **2004**.
(24) Lin, K.; Chang, K.; Hu, C. *Electrochimica Acta* **2009**.
(25) Liu, X. *Journal of Power Sources* **2008**.
(26) Zheng, J.; Cygan, P. *Journal of The Electrochemical Society* **1995**.
(27) Hu, C.; Chang, K.; Lin, M. *Nano Lett* **2006**.
(28) Broughton, J.; Brett, M. *Electrochimica Acta* **2005**, *50*, 4814–4819.
(29) Tsou, T. *Electrochemistry Communications* **2002**.
(30) Rajendra Prasad, K. *Electrochemistry Communications* **2004**.
(31) Reddy, R. *Journal of Power Sources* **2006**.
(32) Zhang, F.; Zhou, Y. *Materials Chemistry and Physics* **2004**.
(33) Cho, S. *Acc. Chem. Res* **2008**.
(34) Frackowiak, E.; Khomenko, V.; Jurewicz, K. *Journal of power ...* **2006**.
(35) Cao, Y. *Chemistry of Materials* **2008**.
(36) Chen, W.; Wen, T. *Electrochimica Acta* **2003**.

(37) Shinomiya, T.; Gupta, V.; MIURA, N. *Electrochimica Acta* **2006**, *51*, 4412–4419.
(38) Ingram, M.; Staesche, H. *Solid State Ionics* **2004**.
(39) Laforgue, A.; Simon, P.; Sarrazin, C.; Fauvarque, J.-F. *Journal of Power Sources* **1999**, *80*, 142–148.
(40) Rudge, A.; Davey, J.; Raistrick, I.; Gottesfeld, S. *Journal of power ...* **1994**.
(41) Cho, S.; Lee, S. *Nanotechnology* **2008**.
(42) Liu, R.; Duay, J. *Chem. Commun.* **2010**.
(43) Balaya, P. *Energy & Environmental Science* **2008**, *1*, 645.
(44) Fischer, A. E.; Pettigrew, K. A.; Rolison, D. R.; Stroud, R. M.; Long, J. W. *Nano Lett* **2007**, *7*, 281–286.
(45) Biswas, S.; Drzal, L. T. *ACS Appl Mater Interfaces* **2010**, *2*, 2293–2300.
(46) Hou, Y.; Cheng, Y.; Hobson, T. *Nano letters* **2010**.
(47) Cottineau, T.; Toupin, M.; Delahaye, T. *Applied Physics A: ...* **2006**.
(48) Chang, J.; Lin, C. *Electrochemistry Communications* **2004**.
(49) Dong, X.; Shen, W.; Gu, J.; Xiong, L.; Zhu, Y.; Li, H.; Shi, J. *J. Phys. Chem. B* **2006**, *110*, 6015–6019.
(50) Fischer, A.; Pettigrew, K.; Rolison, D.; Stroud, R. *Nano Lett* **2007**.
(51) Reddy, A. L. M.; Shaijumon, M. M.; Gowda, S. R.; Ajayan, P. M. *Nano Lett* **2009**, *9*, 1002–1006.
(52) Zhang, H.; Cao, G.; Wang, Z.; Yang, Y.; Shi, Z. *Nano letters* **2008**.
(53) Liu, R.; Duay, J.; Lane, T.; Bok Lee, S. *Physical Chemistry Chemical Physics* **2010**, *12*, 4309–4316.
(54) Liu, R.; Lee, S. B. *J Am Chem Soc* **2008**, *130*, 2942–2943.
(55) Duay, J.; Lee, S. *ACS nano*.
(56) Liang, Y.; Schwab, M. G.; Zhi, L.; Mugnaioli, E.; Kolb, U.; Feng, X.; Müllen, K. *J Am Chem Soc* **2010**, *132*, 15030–15037.
(57) Long, J. W. *Acc. Chem. Res* **2007**, *40*, 854–862.
(58) Eftekhari, A. *Nanostructured materials in electrochemistry - Ali Eftekhari - Google Books*; 2008.
(59) Bhushan, B. *University of Maryland Central Central Authentication Service*; 2004.
(60) Hulteen, J. C.; Martin, C. R. *Journal of Materials Chemistry* **1997**, *7*, 1075–1087.
(61) Lakshmi, B.; Fisher, E.; Martin, C. *Nature* **1998**.
(62) Lee, S. *J Am Chem Soc* **2008**.
(63) Sherrill, S. A.; Duay, J.; Gui, Z.; Banerjee, P.; Rubloff, G. W.; Lee, S. B. *Physical Chemistry Chemical Physics* **2011**, *13*, 15221.
(64) Shi, J.; Sun, C.; Starr, M. B.; Wang, X. *Nano Lett* **2011**, *11*, 624–631.
(65) Fan, Z.; Liu, Y.; Yan, J.; Ning, G.; Wang, Q.; Wei, T.; Zhi, L.; Wei, F. *Adv. Energy Mater.* **2012**, n/a–n/a.
(66) Wang, Y.; Takahashi, K.; Lee, K. H.; Cao, G. Z. *Adv. Funct. Mater.* **2006**, *16*, 1133–1144.
(67) Wang, Y.; Cao, G. *Advanced Materials* **2008**, *20*, 2251–2269.
(68) Hoar, T. P.; Yahalom, J. *Journal of The Electrochemical Society* **1963**, *110*, 614.

(69) Zhang, H. *Journal of The Electrochemical Society* **2005**.
(70) Jessensky, O.; Muller, F.; Gosele, U. *Applied Physics Letters* **1998**, *72*, 1173–1175.
(71) Nielsch, K.; Choi, J.; Schwirn, K.; Wehrspohn, R. B.; Gösele, U. *Nano Lett* **2002**, *2*, 677–680.
(72) O'sullivan, J. In *Proceedings of the royal society of London ...*; 1970.
(73) Keller, F.; Hunter, M. S.; Robinson, D. L. *Journal of The Electrochemical Society* **1953**, *100*, 411.
(74) Thompson, G. E. *Thin Solid Films* **1997**, *297*, 192–201.
(75) Sheasby, P. G.; Wernick, S.; Pinner, R. **1987**.
(76) Masuda, H. *Science* **1995**.
(77) Tian, Y. T.; Meng, G. W.; Gao, T.; Sun, S. H.; Xie, T.; Peng, X. S.; Ye, C. H.; Zhang, L. D. *Nanotechnology* **2003**, *15*, 189–191.
(78) Meng, G.; Jung, Y. J.; Cao, A.; Vajtai, R.; Ajayan, P. M. *Proc Natl Acad Sci USA* **2005**, *102*, 7074–7078.
(79) Shuoshuo, C.; Zhiyuan, L.; Xing, H.; Hui, Y.; Yi, L. *Journal of Materials Chemistry* **2010**, *20*, 1794.
(80) Masuda, H.; Yasui, K. *Advanced Materials* **2000**.
(81) Kyotani, T.; Tsai, L. *Chemistry of Materials* **1996**.
(82) Ko, E.; Choi, J.; Okamoto, K.; Tak, Y.; Lee, J. *ChemPhysChem* **2006**, *7*, 1505–1509.
(83) Li, Y.; Meng, G. W.; Zhang, L. D.; Phillipp, F. *Applied Physics Letters* **2000**, *76*, 2011.
(84) Liu, R.; Cho, S. I.; Lee, S. B. *Nanotechnology* **2008**, *19*, 215710.
(85) Snyder, G.; Lim, J.; Huang, C. *Nature Materials* **2003**.
(86) Ban, S.; Maruno, S. *Biomaterials* **1995**, *16*, 977–981.
(87) Gal, D.; Hodes, G.; Lincot, D. *Thin Solid Films* **2000**.
(88) Chou, S.; Wang, J.; Liu, H. *Journal of Power Sources* **2008**.
(89) Chen, X.; Gerasopoulos, K.; Guo, J.; Brown, A.; Wang, C.; Ghodssi, R.; Culver, J. N. *Adv. Funct. Mater.* **2010**, *21*, 380–387.
(90) Banerjee, P.; Perez, I.; Henn-Lecordier, L.; Lee, S. B.; Rubloff, G. W. *Nature Nanotech* **2009**, *4*, 292–296.
(91) Kemell, M.; Ritala, M.; Leskelä, M. *Microelectronic ...* **2007**.
(92) Elam, J. W.; Libera, J. A.; Pellin, M. J.; Stair, P. C. *Applied Physics Letters* **2007**, *91*, 243105–243105–3.
(93) Biener, J.; Baumann, T. F.; Wang, Y.; Nelson, E. J.; Kucheyev, S. O.; Hamza, A. V.; Kemell, M.; Ritala, M.; Leskelä, M. *Nanotechnology* **2007**, *18*, 055303.
(94) Herrera, J. E.; Kwak, J. H.; Hu, J. Z.; Wang, Y.; Peden, C. H. F. *Top Catal* **2006**, *39*, 245–255.
(95) Kim, G. M.; Lee, S. M.; Michler, G. H.; Roggendorf, H.; Gosele, U.; Knez, M. *Chem. Mater* **2008**, *20*, 3085–3091.
(96) Rugge, A.; Becker, J. S.; Gordon, R. G.; Tolbert, S. H. *Nano Lett* **2003**, *3*, 1293–1297.
(97) Wang, C.-C.; Kei, C.-C.; Perng, T.-P. *Nanotechnology* **2011**, *22*, 365702.
(98) Wang, C.; Kei, C.; Yu, Y. *Nano letters* **2007**.
(99) Perez, I.; Robertson, E.; Banerjee, P.; Henn-Lecordier, L.; Son, S. J.; Lee, S.

B.; Rubloff, G. W. *Small* **2008**, *4*, 1223–1232.
(100) Sneh, O.; Clark-Phelps, R.; Londergan, A.; Winkler, J. *Thin Solid Films* **2002**.
(101) Hoivik, N.; Elam, J. W.; George, S. M.; Gupta, K. C.; Bright, V. M.; Lee, Y. C. In *2002 International Microwave Symposium (MTT 2002)*; IEEE, 2002; Vol. 2, pp. 1229–1232.
(102) Kim, Y.; Sardari, S.; Meyer, M.; Iliadis, A. *Sensors and Actuators B ...* **2012**.
(103) Stoller, M. D.; Ruoff, R. S. *Energy Environ. Sci.* **2010**, *3*, 1294–1301.
(104) Shaijumon, M.; Ou, F.; Ci, L. *Chemical Communications* **2008**.
(105) Chou, S.; Wang, J.; Chew, S.; Liu, H. *... Communications* **2008**.
(106) Rolison, D.; Long, J.; Lytle, J.; Fischer, A. *Chemical Society ...* **2009**.
(107) Reddy, A. L. M.; Shaijumon, M. M.; Gowda, S. R.; Ajayan, P. M. *J. Phys. Chem. C* **2010**, *114*, 658–663.
(108) Kucernak, A. *Electrochimica Acta* **2002**.
(109) Wei, J.; Nagarajan, N. *Journal of Materials Processing ...* **2007**.
(110) Hu, C.-C.; Wang, C.-C. *Journal of The Electrochemical Society* **2003**, *150*, A1079.
(111) Pan, H.; Li, J.; Feng, Y. P. *Nanoscale research letters* **2010**, *5*, 654–668.
(112) Janes, R.; Aldissi, M. *Chem. Mater* **2003**.
(113) Gao, L. *J. Phys. Chem. B* **2005**.
(114) Subramanian, B.; Jayachandran, M. *Materials Letters* **2008**, *62*, 1727–1730.
(115) Elam, J.; Schuisky, M.; Ferguson, J. *Thin Solid Films* **2003**.
(116) Frackowiak, E. *Physical Chemistry Chemical Physics* **2007**.
(117) Cao, G.; Yang, Y. *Energy & Environmental Science* **2009**.
(118) Lota, G.; Fic, K.; Frackowiak, E. *Energy & Environmental Science* **2011**, *4*, 1592–1605.
(119) Im, J.; Kim, S.; Kang, P. *... of Industrial and Engineering Chemistry* **2009**.
(120) Jiang, L.; Gao, L. *Journal of Materials Chemistry* **2005**, *15*, 260.
(121) Ge, C.; Armstrong, N. R.; Saavedra, S. S. *Anal. Chem.* **2007**, *79*, 1401–1410.
(122) Weinstein, L.; Yourey, W.; Gural, J.; Amatucci, G. G. *Journal of The Electrochemical Society* **2008**, *155*, A590.
(123) Putkonen, M.; Harjuoja, J.; Sajavaara, T.; Niinist, L. *Journal of Materials Chemistry* **2007**, *17*, 664.
(124) Andricacos, P. *The Electrochemical Society Interface* **1999**.
(125) Leskelä, M. *Thin Solid Films* **2002**.
(126) Kucheyev, S. O.; Biener, J.; Baumann, T. F.; Wang, Y. M.; Hamza, A. V.; Li, Z.; Lee, D. K.; Gordon, R. G. *Langmuir* **2008**, *24*, 943–948.
(127) Elam, J.; Zinovev, A.; Han, C.; Wang, H.; Welp, U. *Thin Solid Films* **2006**.
(128) McEvoy, T. M.; Long, J. W.; Smith, T. J.; Stevenson, K. J. *Langmuir* **2006**, *22*, 4462–4466.
(129) Wang, Y.; Li, H. *Advanced Materials* **2006**.
(130) Hoppe, H.; Glatzel, T.; Niggemann, M.; Schwinger, W. *Thin Solid Films* **2006**.
(131) Sakamoto, J. S.; Dunn, B. *Journal of Materials Chemistry* **2002**, *12*, 2859–2861.
(132) Kim, H.; Han, B.; Choo, J.; Cho, J. *Angewandte Chemie* **2008**, *120*, 10305–10308.
(133) Wood, G.; O'sullivan, J.; Vaszko, B. *Journal of The Electrochemical Society*

1968, *115*, 618.
(134) Furneaux, R.; Rigby, W.; Davidson, A. *Nature* **1989**.
(135) Nielsch, K.; Muller, F.; Li, A. *Advanced Materials* **2000**.
(136) Platschek, B.; Petkov, N.; Himsl, D.; Zimdars, S.; Li, Z.; Köhn, R.; Bein, T. *J Am Chem Soc* **2008**, *130*, 17362–17371.